DESIGN AND SIMULATION OF A PRESSURE WAVE SUPERCHARGER FOR A SMALL TWO-STROKE ENGINE

THESIS

Mark R. Mataczynski, 2nd Lieutenant, USAF

AFIT-ENY-14-M-34

DEPARTMENT OF THE AIR FORCE
AIR UNIVERSITY

AIR FORCE INSTITUTE OF TECHNOLOGY

Wright-Patterson Air Force Base, Ohio

AFIT-ENY-14-M-34

DESIGN AND SIMULATION OF A PRESSURE WAVE SUPERCHARGER FOR A SMALL TWO-STROKE ENGINE

THESIS

Presented to the Faculty

Department of Aeronautics and Astronautics

Graduate School of Engineering and Management

Air Force Institute of Technology

Air University

Air Education and Training Command

In Partial Fulfillment of the Requirements for the

Degree of Master of Science Aeronautical Engineering

Mark R. Mataczynski, BS

2nd Lieutenant, USAF

March 2014

DISTRIBUTION STATEMENT A.
APPROVED FOR PUBLIC RELEASE; DISTRIBUTION UNLIMITED.

AFIT-ENY-14-M-34

DESIGN AND SIMULATION OF A PRESSURE WAVE SUPERCHARGER FOR A SMALL TWO-STROKE ENGINE

Mark R. Mataczynski, BS

2nd Lieutenant, USAF

Approved:

//signed//	10 March 2014
Marc D. Polanka, PhD (Chairman)	Date
//signed//	10 March 2014
David Liu, Captain, USAF (Member)	Date
//signed//	10 March 2014
Paul I. King, PhD (Member)	Date

AFIT-ENY-14-M-34

Abstract

As small, Remotely Piloted Aircraft become more prevalent as aerial observation platforms in the modern era, there will continue to be a desire to improve their capabilities. The lowered pressures associated with high altitude have an adverse impact on the performance of the small engines that are commonly used to propel small aircraft. The most desirable method of recovering the performance lost as a result of engine operation at high altitude is the integration of a forced induction device. Due to its unique characteristics, a special type of wave rotor called a Pressure Wave Supercharger has the potential to avoid many scaling-related losses, allowing it to operate efficiently as a forced induction device for small engines. This thesis outlines the successful design and computational simulations performed in the development of a Pressure Wave Supercharger for a 95 cc Brison engine. A NASA quasi one-dimensional CFD code was used to produce computational predictions for the performance of a Comprex® Pressure Wave Supercharger and compare these predictions against the measured performance. This code was then used to design a scaled down Pressure Wave Supercharger for use on the 95 cc Brison. This design was modeled using Computer Aided Design and the parts were manufactured. A test rig was also designed for the purpose of testing the scaled Pressure Wave Supercharger. This device will improve the performance of small two-stroke engines flying at high altitudes by boosting the intake manifold pressure to one standard atmosphere or better. This will allow small unmanned aerial systems operated by the Air Force to function at higher altitudes, thus improving their capabilities and mission effectiveness.

iv

Acknowledgments

I would like to express my sincere appreciation to my faculty advisor, Dr. Marc Polanka, for his guidance and support throughout the course of this thesis effort, as well as my thesis committee members, Dr. Paul King and Captain David Liu. I would, also, like to thank the Air Force Research Lab and all of the helpful people who work there, and for the support that they provided to me during this project.

<div align="center">

Mark R. Mataczynski

</div>

Table of Contents

List of Figures

List of Tables

Nomenclature

A	Area
A_a	Inner area of the venturi inlet
A_{AI}	Area of the air inlet port
A_{AO}	Area of the air outlet port
A_b	Area of the venturi throat
A_{eff}	Effective area
a	Speed of sound
C	Discharge coefficient
D	Engine displacement
g_c	Gravitational constant
h	Cell height
L_{cold}	Rotor length at room temperature
L_{hot}	Rotor length at elevated temperature
$\dot{m}$	Mass flow rate
$\dot{m}_{AI}$	Mass flow rate through the air inlet port
$\dot{m}_c$	Corrected mass flow rate
N	Engine speed
P_{ref}	Reference pressure
P_s	Static pressure
P_t	Total pressure
R	Ideal gas constant
r	Radius
Re_x	Reynolds number based on length
T	Static temperature
T_{ref}	Reference temperature
T_s	Time for eighteen pressure wave reflections to traverse a rotor channel
T_t	Total temperature
t	Webbing thickness
t_s	Time for a single pressure wave to traverse a rotor channel
u	Velocity
$\dot{V}$	Volumetric flow rate
w_{avg}	Average cell width
x	Length
γ	Ratio of specific heats
Δ	Differential
δ^*	Displacement thickness
η_v	Volumetric efficiency
ρ	Density
ω	Angular velocity of the rotor

List of Abbreviations

ABB	Asea Brown Boveri
AFIT	Air Force Institute of Technology
AI	Air Inlet
AO	Air Outlet
BBC	Brown Boveri Company
CAD	Computer Aided Design
CFD	Computational Fluid Dynamics
COTS	Commercial off the Shelf
DOD	Department of Defense
EFI	Electronic Fuel Injection
EGR	Exhaust Gas Recirculation
EI	Exhaust Inlet
EO	Exhaust Outlet
ESC	Electronic Speed Controller
GRC	Glenn Research Center
MAP	Manifold Absolute Pressure
NASA	National Aeronautics and Space Administration
PWS	Pressure Wave Supercharger
RPA	Remotely Piloted Aircraft

DESIGN AND SIMULATION OF A PRESSURE WAVE SUPERCHARGER FOR A SMALL TWO-STROKE ENGINE

I. Introduction

I.1 General Issue

The last ten years has shown a marked increase in the use of Remotely Piloted Aircraft (RPA). During this time, RPAs have been used in a multitude of applications from high-endurance passive observation, to active weapons delivery. In order to drive down costs, the engines selected to be used for these aircraft are usually commercially available products manufactured by a civilian company. One of the most challenging issues facing these small engines is the degradation of performance corresponding to engine operation at altitude, where the ambient air pressure and air density are much lower than at sea level. This drop in intake Manifold Absolute Pressure (MAP) corresponds to a loss of crankshaft torque and horsepower that causes performance to suffer for nearly all aircraft maneuvers at altitude. Since RPAs regularly operate at altitudes of 10,000 feet or greater, the loss of performance for decreased MAP is a critical issue that can have undesirable effects on mission performance and capability.

One solution to mitigate the effects of decreased MAP is to improve the fuel delivery system. The two-stroke engines typically used for small RPAs often use carburetors as the method of delivering fuel. Converting the fuel system to an electronically controlled fuel injection system has been shown to improve fuel economy as well as torque and power delivery to the crankshaft at altitude as demonstrated by Crosbie et al. [1], and Husaboe et al. [2]. Since an Electronic Fuel Injection (EFI) system can adjust the rate of

fuel delivery for a wide range of engine loads and conditions, a properly integrated EFI system can improve engine efficiency and power delivery over that of a carburetor for nearly any condition [1, 3]. Implementing this solution would require purchasing an assortment of new sensors and a new electronic control module for each engine, but would remain relatively affordable. The main challenge with this method would be the installation and tuning support from an engineer that knows the system. Since carburetors are much easier to tune with much less expensive tools than an Electronic Fuel Injection system, the cost of the parts alone may be overshadowed by the detrimental effects of added complexity.

Another option to compensate for lost performance would be to design an engine for each RPA that performs optimally for the weight of the aircraft and the range of altitudes and flight conditions in which the aircraft operates. This solution would be theoretically ideal since the engine would be custom-designed for the desired mission performance. However, the costs in research and development as well as manufacturing of the engine would be excessively high. Establishing a cost-effective process with the proper supporting infrastructure to manufacture the hundreds of engines required by the Air Force would entail a massive expenditure of resources only after a long, costly acquisition process. Since the facilities and machinery used to accomplish this task would become obsolete after the required few hundred engines had been manufactured, this process would lead to far more waste than is justifiable. In the current fiscal climate that the Department of Defense (DOD) must operate in, controlling and reducing costs is a high-emphasis item that rules out a custom designed engine for each RPA.

A third potential solution for dealing with lower ambient pressures is to simply increase the pressure ratio from the ambient air to the intake manifold air. The most prevalent method of accomplishing this is the implementation of a turbo-normalization device such as a turbocharger or supercharger. Turbo-normalization takes energy from the engine crankshaft or waste exhaust gasses and uses it to operate a compressor [3]. Air at ambient pressure is passed through the compressor where the pressure is increased with the intended purpose of increasing the overall mass flow rate of air to the intake manifold. For a small two-stroke engine that has little excess energy to spare for the operation of a compressor, the power relative to the overall output of the engine that would be needed to operate a conventional turbo-normalization device is often excessive. Superchargers and turbochargers with their supporting systems are often complex and expensive to implement for a small engine [3]. However, one turbo-normalization device called a wave rotor, or Pressure Wave Supercharger (PWS), requires less energy from the engine to operate than a conventional supercharger [4]. Scaling down of a conventional turbo-normalization device also entails large losses that could potentially be less significant for a PWS. For these reasons as well as a multitude of other advantages to be discussed in this paper, a PWS was chosen as the design focus of this research project.

I.2 Objectives

The overall objective of this research was to properly design a special type of supercharger called a Pressure Wave Supercharger that is sized for a small-bore 95 cc Brison engine and to validate the design by constructing a test apparatus for the purpose of

measuring the mass flows, pressures, and temperatures at the relevant locations. In order to accomplish this goal, the project was split into four major tasks.

1. Improvement of the test apparatus of Smith et al. [5] for the purpose of further Comprex® PWS testing with improved temperature capability

2. Validation of the NASA GRC CFD code developed by Paxson [6] applied to a reverse-flow wave rotor of the type designed in this project

3. Theoretical design and computational simulation of a small scale PWS sized for the 95 cc Brison engine

4. Manufacturing, and mechanical integration of the scaled PWS into a test apparatus for the purpose of testing the scaled model against the CFD code used

I.3 Methodology

While each task within the overall project was related to the other tasks, they each required their own specific set of procedures in order to accomplish them. This section will outline the basic methods performed to accomplish each task. These procedures will be covered in much greater detail and depth throughout Chapters III and IV.

Since Smith et al. [5] were only able to achieve a temperature in the exhaust inlet tube of 883 R during testing, it was desired to improve the current facility's temperature capability in order to test the Comprex® wave rotor at higher temperatures. This was important because the diesel engine that the Comprex® was designed for usually operated with exhaust gas temperatures of approximately 1500 R. Although temperatures this high

4

were not achieved in testing, the effect of the exhaust inlet temperature was quantified for the Comprex®. The results of these tests will be further discussed in Chapter IV.

The next step of the project involved using a Computational Fluid Dynamics (CFD) code developed by Paxson et al. [6] at the NASA Glenn Research Center. This code was originally written specifically for the purpose of simulating the performance of wave rotors used as a turbine topping cycle, and not as a supercharger. For this project, this code was used to simulate the Comprex® PWS that was tested in the first part of this project. The code was able to predict the mass flows to each port of the Comprex® when comparing experimental data to the calculations performed by the code to within 4.2%. This accuracy was deemed good enough to validate the use of the code as a design tool for the proposed small-scale Pressure Wave Supercharger of this project. The results of these simulations and their accuracy will be discussed in further detail in Chapter IV.

The first step in the design process of the scaled rotor was to learn how to use the NASA Glenn Research Center quasi-one-dimensional Computational Fluid Dynamics code for design purposes. Calculations were performed in an excel spreadsheet in order to determine the proper geometry of a rotor designed to provide sufficient mass flow for the Brison engine. The code was then run and slight changes were made to the input file regarding the pressures at the air outlet and exhaust inlet ports of the wave rotor, as well as the flow area in the air outlet line that was controlled using a simulated valve that is present on the actual test facility. These parameters were changed until the simulation indicated that the mass flows were balanced for proper and realistic operation of the PWS, and the mass flow that the device was designed to supply to the engine was achieved. Calculations

of the mass flow demanded by the engine partially determined the physical geometry of the rotor and allowed the design process to move forward to the Computer Aided Design (CAD) modeling phase.

For the fourth part of the project, the parts of the wave rotor machine and the supporting test facilities were designed or selected in order to ensure proper working order and assembly of the overall device. The assembly feature was used in SolidWorks to detect potential interference between the parts in the machine, and to demonstrate a feasible method for mounting the rotor and shaft with the stationary endwalls, shroud, and supporting instrumentation. Direct metal laser sintering was selected as the most cost-effective method for manufacturing the rotor and endwalls, as these parts would be excessively difficult to machine from a solid piece of material. A test facility was also designed and is currently under construction in order to facilitate the testing of the scaled PWS and compare the resulting data to the predictions of the CFD code.

Using the small-scale testing apparatus, multiple test points will be tested on the scaled wave rotor and compared to the CFD output from the NASA GRC code. This data will aid the validation of the CFD code for use on any small scale wave rotor, as the code has only been utilized and validated for rotors of much larger volume and size than the one used in this project. One of the objectives of conducting this research was to prove or disprove the theory that a small PWS would effectively avoid most of the scaling-related performance issues that plague conventional turbochargers and superchargers for small engines. The scaled testing facility will eventually indicate the scale of the losses present

in such a small-scale PWS, and determine whether or not the implementation of such a device will be feasible for small engines.

II. Background and Previous Research

The objective of conducting this research was to design a Pressure Wave Supercharger that is properly sized for the 95 cc Brison engine in order to improve the performance of that engine while operating at high altitude. The Brison engine was chosen because the engine is a Commercial off the Shelf (COTS) product that is used in RPAs operated today, and it is of a representative size of many of the other small two-stroke engines used for small RPAs. The Brison was also a suitable candidate since Husaboe et al. [2] at the Air Force Institute of Technology (AFIT) had previously gathered data on this particular engine's performance at multiple simulated altitudes and demonstrated the engine's loss of performance for decreased MAP. Successful design of a PWS for this engine could eventually lead to integration and testing on the real engine, so having a well-established baseline for the performance of the Brison engine is a huge advantage.

Since the Comprex® was a commercially successful device that has been utilized as a supercharger for multiple internal combustion engines, it was chosen as the starting point of the design philosophy for the smaller rotor. Prior research by Smith et al. [5], and Hirecaga et al. [7] suggests that scaling down of a PWS can result in a device that is more efficient than conventional forced induction methods of similar size. The method used in this project to validate this idea theoretically was through the use of Computational Fluid Dynamics. This tool allows the designer to modify the boundary conditions of the rotor in order to account for the losses and other challenges associated with running a PWS at such a small scale. The CFD code itself has been used in the past to predict the performance of the Comprex® [5], validating its utility and accuracy as a simulation and design tool. Once

the scaled down wave rotor had been designed, the endwalls had to be properly modeled

in CAD along with the shroud and bearings to ensure proper fitment of all parts. Next, the

parts were manufactured and a test rig similar to that of Smith et al. [5] was designed and

built for the purpose of testing the scaled PWS. In order to illustrate the importance of this

project, the remainder of this chapter will discuss the history of wave rotor technology as

well as the problems associated with modern turbochargers and superchargers that make

this project relevant.

II.1 Pressure Wave Supercharger Advantages

Many commercially available options already exist to increase the MAP for small

engines. The most common options for increasing the intake charge pressure of an internal

combustion engine are conventional turbochargers and superchargers. Examples of a

conventional turbocharger and a conventional screw type supercharger are depicted in

Figure 1 and Figure 2, respectively.
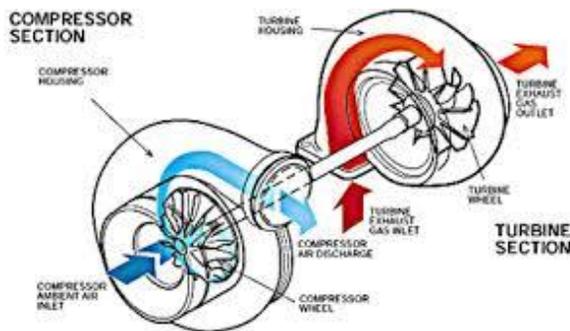
Figure 1: Conventional turbocharger
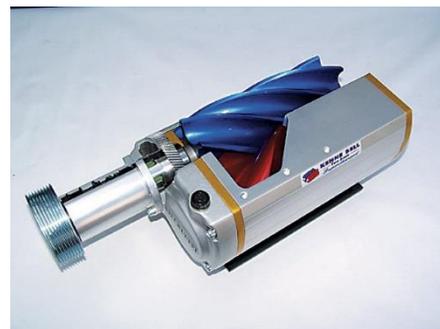
Figure 2: Conventional supercharger

A supercharger is operated by mechanically linking the compressor to the crankshaft of the engine by use of a pulley. The power derived from the crankshaft is used by the compressor to increase the intake manifold pressure, thus improving engine power. A turbocharger is a type of supercharger that uses the exhaust gasses from the engine to drive a turbine that is linked via a shaft to a centrifugal compressor which feeds compressed air to the intake manifold. Both of these devices are not without cost, however. The large physical size of most superchargers corresponds to high spatial requirements and excessive weight. Superchargers are also generally much less efficient and provide a lower boost in MAP than turbochargers of similar size [3]. These factors realistically rule out the use of a supercharger for a small aircraft. Turbochargers often require an intricate system of exhaust piping and intake piping in order to direct the flow of the exhaust gas and intake air through the turbine and compressor, respectively. The piping, the turbine, and the compressor all take up a large amount of space and are usually quite heavy, though typically smaller and lighter than a supercharger. Since RPAs do not carry a pilot, these small aircraft are usually designed to be light-weight with minimal space for excess machinery in the engine compartment. Weight requirements make incorporating a turbocharger into a small engine system difficult, but more favorable than using a supercharger.

According to Doerfler [4], the relatively small exhaust gas mass flows associated with engine operation at low engine speeds can be insufficient for spinning the turbine fast enough to create sufficient compression and air density from the compressor. Both types of systems generally utilize an intercooler in order to reduce the intake charge temperature, adding more weight to the system. A PWS was chosen for this project because of its several

advantages over a conventional supercharger or turbocharger. The history of the development of the PWS as well as the differences and advantages of a PWS over conventional forced induction devices will be discussed later in this section. The PWS designed for his project is the first such device that has been designed and tested for an engine as small as the 95 cc Brison. The design process used to develop this wave rotor will be discussed later on in the paper.

Conventional turbochargers and superchargers each have distinct advantages and disadvantages relative to one another as well as a PWS. A mechanical supercharger, for example, provides a boost in MAP with excellent response time since it is driven directly from the crankshaft. Since the power taken from the crankshaft is used to spin the supercharger and do the work needed to compress the air, mechanical superchargers for small engines generally require a high amount of power as a percentage of overall engine power to operate [3]. Furthermore, the gain in MAP from a supercharger is generally relatively low since spinning the compressor at a high enough speed to provide further compression would require a high pulley ratio from the crankshaft to the supercharger, resulting in a large amount of friction loss. Since the small reconnaissance-type aircraft in question run on very small two-stroke engines with limited power, drawing a large amount of excess power from the crankshaft to run a compressor can seriously bog the engine down for low speed operating conditions [8]. Superchargers are also generally heavy machines that take up a large amount of space compared to the overall engine. This is not always a cause for concern for an automobile engine where space and weight are less of a concern. For an aircraft that needs to be as light as possible to fly, weight and space are a huge

concern. Superchargers also do not create back pressure in the exhaust system. For a two-stroke engine, evacuation of the exhaust gases from the previous cycle occurs at the same time as the scavenging of the intake air/fuel mixture. Without back pressure to balance out the exhaust side of the cylinder, a supercharged intake air/fuel mixture at high pressure is likely to be largely blown right through the cylinder and wasted. Because of these constraints, the use of a supercharger for the application in question of a small aircraft with a 95 cc two-stroke engine does not make sense.

Unlike superchargers, turbochargers do not require crankshaft power to operate. A turbocharger works by removing energy from the exhaust gases to spin a turbine at high speed. This turbine is mechanically linked to a compressor via a shaft. The spinning of the centrifugal compressor draws air into the impeller and increases the flow velocity through rotation. The flow is then decelerated and compressed in the diffuser and collected by the compressor manifold and ducted to the intake manifold [9]. For the compression ratios of 3:1 and lower that are typically used for superchargers applied to automobile engines, this single-stage compression design allows for typical efficiencies of up to 80% in modern turbochargers. For small engines that produce relatively small exhaust gas mass flows, spinning a turbine fast enough to create significant compression becomes a challenge [4]. These small mass flows can also cause the lag time between throttle demand and compressor spool to be large. Unlike a supercharger, the turbine in a turbocharger does create back pressure in the exhaust system, making the implementation of a turbocharger to a small two-stroke engine more practical than a supercharger. These factors make turbochargers a more realistic solution for increasing the MAP of a small two-stroke.

While a turbocharger represents a viable solution with some gains for boosting a small two-stroke engine, a PWS sized for the same engine can outperform a turbocharger if the wave rotor is properly designed. Compared to a turbocharger, the throttle response lag time is significantly reduced as shown in Figure 3. Since the compression process depends on pressure waves moving at the speed of sound, the time it takes for the PWS to begin producing compressed intake air is short. Conversely, the turbocharger must take more lag time in order to spool as the inertia of the compressor and turbine must be overcome. A comparison of lag time between a Comprex® PWS and a turbocharger is depicted in Figure 3. Although a large turbocharger or a multiple stage turbocharger could theoretically provide a pressure ratio of 3:1 that a single PWS is capable of providing, this would add weight and complexity to the system [8]. Since the compression efficiency across a shock wave is higher than that of a compressor blade, the PWS has the potential to be much more efficient than a typical compressor as shown in Figure 4.
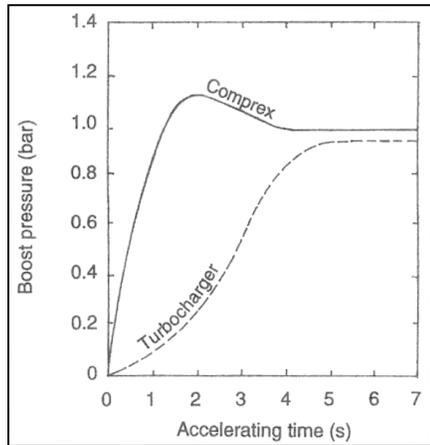
Figure 3: Lag time comparison of a PWS vs. a turbocharger [4]
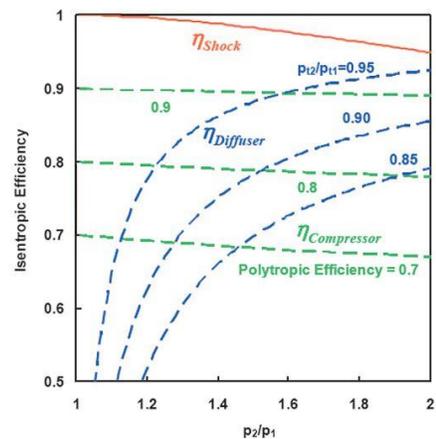
Figure 4: Isentropic efficiency of shock waves vs. compressor [4]

The overall efficiency of the device is based on the isentropic efficiency of a shock wave as well as the losses due to flow leakage and bearing friction. The overall efficiency of a turbocharger is subject to bearing friction and leakage as well, but the efficiencies of the compressor, diffuser, and turbine must also be taken into account. Tests conducted by the Brown Boveri Company (BBC) of their Comprex® device has resulted in maximum compression efficiencies of 75%, and lower emissions than engines with conventional turbochargers [10]. While a limited amount of built in Exhaust Gas Recirculation (EGR) helps to reduce NO_x emissions significantly and improve efficiency, too much EGR can lead to starving the engine of the air it needs to run. Engines with EGR typically experience approximately 2-5% higher thermal efficiency (for limited EGR) as compared to an engine with no EGR [11]. However, modifications made to the endwalls of the Comprex® device has resulted in nearly complete cancellation of excessive EGR at full load engine operation.

The much higher efficiencies observed for a PWS sized to a 2.0 Liter automobile engine compared to similarly scaled down conventional superchargers suggest that further downscaling could lead to even greater efficiency advantages [12]. It is the desire for more efficient small turbomachinery in small engines that may justify the selection of a PWS as a method of increasing the MAP of the Brison engine to improve its performance at altitude. The goal of this study is to design a PWS that is properly scaled for the 95 cc Brison engine in order to assess its potential as a worthwhile supercharging device. If the expected benefits in efficiency and pressure gain can be observed in eventual testing, it may eventually be possible to mate the device with the actual engine and perform further testing and analysis.

II.2 History of the Pressure Wave Supercharger

The earliest proposal of a device resembling a PWS occurred in 1906 in a British patent by Knauff [13]. Although he initially described a machine with curved passages with the intention of extracting power from the pressure exchanges occurring in the channels, Knauff's first physical machine was of the form of a cylindrical drum with straight axial passages rotating between two endplates. Flows of different pressures entering and leaving the passages exchanged pressure through a process not involving pressure waves. It was not until around 1928 that Burghard, based largely on the work of Knauff and others, proposed the utilization of pressure waves to exchange pressure in a device he termed a "dynamic pressure exchanger." A dynamic pressure exchange involves both compression and expansion processes occurring within the axial channels. This utilization of pressure waves is what leads to the term "wave rotor."

The Brown Boveri Company, or BBC, (later Asea Brown Boveri [ABB]) was one entity that was largely responsible for the commercial development and eventual implementation of the wave rotor as a performance enhancing machine [4]. In 1940, BBC designed a wave rotor as a topping cycle for a British Railways locomotive gas turbine. Although the device tested well, it did not perform as desired when mated to the actual turbine. The successful testing of the machine did, however, prove that the concept of a wave rotor could theoretically be used successfully in conjunction with a gas turbine as a performance enhancing machine. The limited success of this prototype and further

development eventually led to the conception of using a wave rotor as a Pressure Wave Supercharger for automobile diesel engines [13].

The first successful Pressure Wave Superchargers were manufactured and tested on diesel engines between 1947 and 1955 by the ITE Circuit Breaker Company and the U.S. Bureau of Aeronautics [14]. This led to BBC, already a manufacturer of automobile superchargers at the time, to invest in the research and development of a PWS for diesel engines. BBC succeeded in developing these devices with effective implementation of a PWS on a truck diesel engine in 1971, and then again later with a model developed for a 2.1 L passenger car engine in 1978 [13]. The passenger car model was given the trade name Comprex®. The Comprex® was later implemented as a widely used commercial product as a supercharger for the Mazda 626 Capella 2.0 L diesel engine starting in 1987. Since then, the primary development of the wave rotor has been focused on use as a topping stage for a turbine cycle according to Akbari and Nalim [13].

The Comprex® is the most famous example of a wave rotor that was successfully offered as a commercial product. In the late 1980's, the Mazda 2.0 L diesel equipped with a Comprex® supercharger was able to produce around 75 total peak horsepower, not very powerful by today's standards for a supercharged engine of that size. However, wave rotors have also been tested in much more powerful engines. One interesting example of this came in the form of experimentation by the Ferrari Formula 1 team in 1981 when they tested their 126 CX chassis equipped with a Comprex® supercharger. The engine used was a 1.5 L V6 engine that produced 570 peak horsepower at 11,500 rpm [15]. The Comprex® was fitted to the engine for testing purposes but it was determined that the twin-turbo setup

would make it easier to optimize the performance of the racing engine, and the Comprex®
was never equipped on the car for a race.

Since the use of Computational Fluid Dynamics has become prevalent in the
aerodynamics community, the CFD and the development of computational methods
specifically for wave rotors has also become a primary focus for much of the current
research being conducted pertaining to wave rotors [6]. CFD codes used for predicting
wave rotor performance generally use a mathematical method to solve the Navier-Stokes
equations for the flow inside the channels of the rotor. Because shock waves are present in
the channels, the method chosen must be able to account for the discontinuity across the
shock. Because of this, an exact solution is very difficult to find, so some kind of iterative
method is usually employed. Since the process in the channel is repetitive, the conditions
at the beginning of the cycle must match the conditions at the end of the cycle. A more in-
depth discussion of the CFD code used for this project is included in Section II.5.

II.3 Different Types of Wave Rotors

Although this paper focuses on the use of a wave rotor as a supercharger for an
internal combustion engine, there are many different types of wave rotors spanning a wide
range of purposes. From the first concept of a wave rotor as a self-contained engine to wave
rotors as turbine topping cycles, each different application yields a slightly different design.

The use of a wave rotor as an engine to produce power became a reality when
Pearson successfully designed, manufactured, and tested his Pearson rotor sometime in the

mid-1950s to 1960s [13]. Pearson's rotor was designed using complex wave diagrams based on the use of the method of characteristics. His design accounted for internal shock wave reflections and incorporated multiple devices to cancel out unwanted reflections in key areas. The Pearson rotor achieved promising results with several hundred hours of successful operation with thermal efficiencies of around 10% and a power output of around 35 hp at the design point for a device that was of a 9 inch diameter by 3 inches in length. The device was eventually destroyed due to over speeding and the project was cancelled when additional funding could not be secured [16].

Wave rotors have also been developed for use as a turbine topping cycle as depicted in Figure 5. These types of wave rotors work by running air from a compressor through the wave rotor to further compress the flow before it is directed to the combustor. The enthalpy gained from the combustor is then used to compress the fresh incoming air from the compressor as the high pressure gas from the combustor flows through the wave rotor. This allows combustion to occur at a higher pressure and temperature than it otherwise would, and the total pressure of the gas at the inlet of the turbine is increased above that of the air at the exit of the compressor. In an un-topped cycle, total pressure is usually lost in the combustor due to incomplete combustion and other inefficiencies in the flow. The topped cycle allows comparatively higher total pressures at the turbine inlet than an engine without a topping stage, while maintaining approximately the same turbine inlet temperature due to cooling within the wave rotor as the flow expands through the channel [17]. Due to the fact that the cold air runs through the rotor during the compression process (as does the hot gas coming through during the expansion process), this type of device is called a through-

flow wave rotor. Since the colder air from the compressor passes all the way through each channel as it rotates past the air inlet port, this type of wave rotor is self-cooling and because of this will maintain a fairly constant rotor temperature.
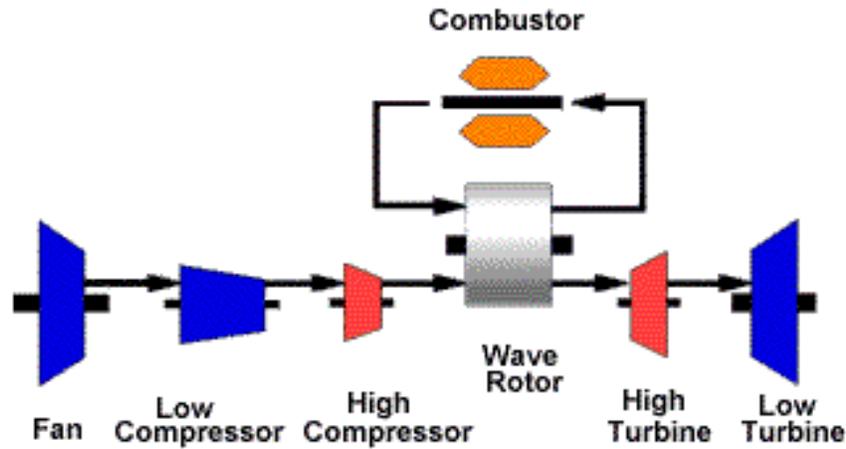
Figure 5: Diagram of a through-flow wave rotor applied as a turbine topping cycle

While through-flow wave rotors are used for turbine engines, a different type of wave rotor may be used for a lower temperature application where cooling is less important and the temperatures experienced are not close to the melting point of the materials in the rotor. For this reason as well as spatial considerations, reverse-flow wave rotors are often used in Pressure Wave Supercharger applications. In a reverse-flow wave rotor, both the cold air and the hot gas enter and exits the rotor on the same respective side. This results in a relatively cooler side (the cold side) for the side that the inlet air is on, and a relatively hotter side (the hot side) for the side of the exhaust gases. The results of the process are much the same, although the self-cooling properties of a through-flow wave rotor are no longer applicable. Air enters the wave rotor and is compressed by a series of shock wave

interactions that will be discussed in more detail later in section II.4. The compressed air is then forced out of the air outlet port and supplied to the intake manifold, just like any supercharger. One advantage of using a reverse-flow wave rotor is that the piping for the exhaust gases remains on one side of the device while the piping for the intake air remains on the opposite side. This is beneficial to avoid overly intricate exhaust piping and intake piping configurations that would take up an unnecessary amount of space. Another advantage of this configuration has to do with the position of the bearings. Since the rotor is only supported on the cold side of the device, the heat load on the rotating components and most importantly the heat load on the bearing are greatly reduced. Since there will be a constant flow of cool intake air around the bearing holders, the heat load on the bearings should be greatly reduced.

II.4 Internal Workings of a Pressure Wave Supercharger

A conventional turbocharger for an automobile engine compresses air by the use of a centrifugal compressor that is driven by a shaft connected to a turbine. The turbine is driven by the energy of exhaust gases from the engine that would otherwise be largely wasted [3]. A PWS achieves compression of a gas in a different manner. A PWS is an unsteady flow machine that utilizes shock wave interactions in a single rotor cell between a high pressure driver gas and a low pressure driven gas to equalize the pressure of the two gases. This leads to the development of two processes within the rotor; compressing and scavenging. The compression process is the increase in pressure of the low pressure gas (in this case, air) due to the shock wave pressure equalization between the low pressure gas

and the high pressure gas (exhaust gas). The scavenging process involves the scavenging of the high pressure gases from the rotor channels through the use of expansion waves in order to enable more low pressure fluid to be drawn into the channel [13].

There are four main components to a PWS; the rotor, the shroud, and two endwalls (Shown in Figure 6). The rotor is a single part contained within the shroud that consists of one or two rows of axially aligned channels at a specific radius as shown in Figure 7 below.
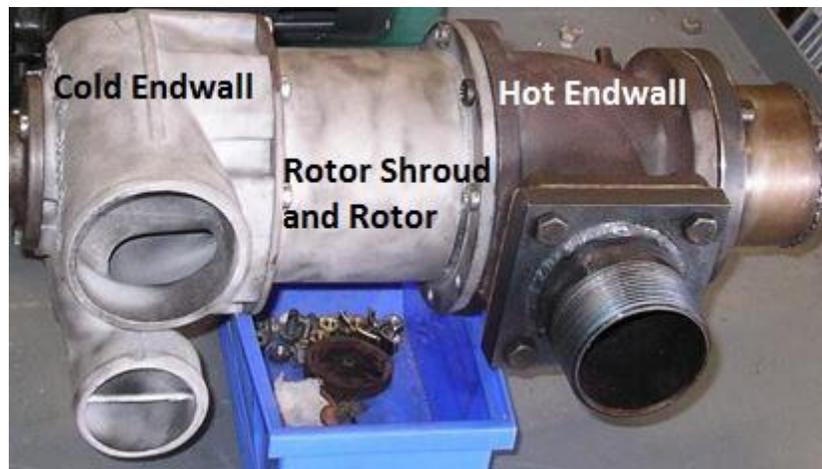
Figure 6: Assembled Comprex® PWS
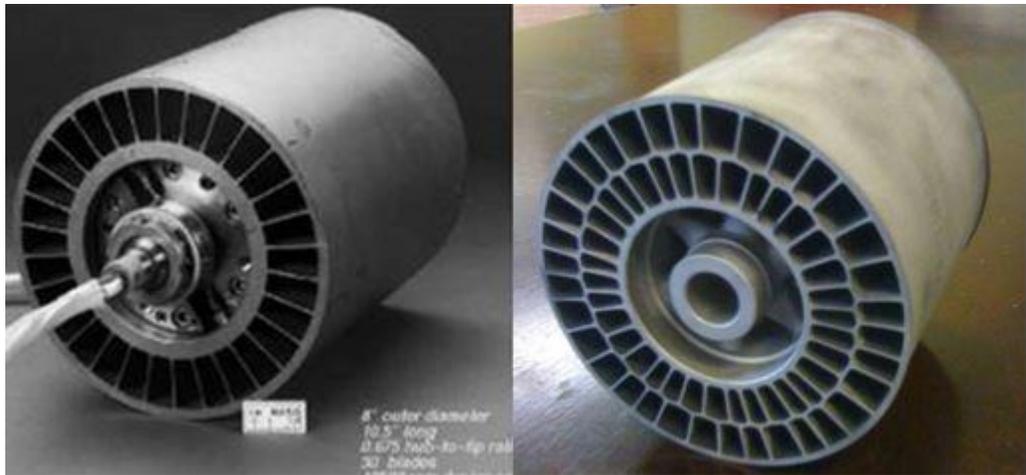
Figure 7: Two different rotor designs

The rotor spins about the axis of a support shaft that is mated to the cold side of the rotor. This shaft is supported by two bearings mounted in one of the stationary endwalls. The endwalls sit on either side of the rotor, with a cold side endwall for directing the intake air and a hot side endwall for directing the exhaust gases. The shroud connects the two endwalls to each other and encloses the spinning rotor. The shroud is designed to prevent leakage from the rotor by keeping the ends of the rotor as close as possible to the face of each endwall. As the rotor spins, each channel acts in a similar way as a shock tube with a series of shock waves or pressure waves being generated by high pressure endwall pockets, and expansion fans generated by low pressure endwall pockets running through the length of the rotor. A shock tube is a laboratory device that creates a strong shock in a long pipe that generates variable pressures along the pipe resulting from shock waves and expansion waves as they reflect off of the walls at either end of the pipe [18].

The type of PWS used for increasing the intake charge pressure in an automobile is a reverse flow wave rotor. For a reverse flow type wave rotor, each cycle of the compression process begins with the opening on the hot side of the rotor channel passing by the exhaust outlet (EO) port of the hot side endwall (1, Figure 8). This rapid opening of the relatively low pressure EO port creates an expansion fan that propagates down the length of the channel and lowers the pressure in the channel while drawing exhaust gases out of the EO port. As the opening on the cold side of the rotor channel passes by the air inlet (AI) port of the cold side endwall (2, Figure 8), the decreased pressure in the channel allows cold intake air to flow into the channel. The closing of the EO port on the hot side then creates a weak pressure wave (3, Figure 8) that propagates along the channel and reaches the cold side of the rotor just as the AI port closes and traps the gas as it is compressed by the pressure wave. The rotor then rotates further and the hot side of the rotor passes by the exhaust inlet (EI) port on the hot side endwall. The rapid introduction of the high pressure exhaust gas from the EI port creates a strong pressure wave (4, Figure 8) that compresses the air even further. Around the time the pressure wave reaches the cold side of the rotor, the air outlet (AO) port opens and the high pressure air in the channel is forced into the AO port where it is directed to the intake manifold (5, Figure 8). Once most of the air has evacuated the channel, the AO port closes to avoid ingesting the exhaust gases that have mixed with the compressed air [17].
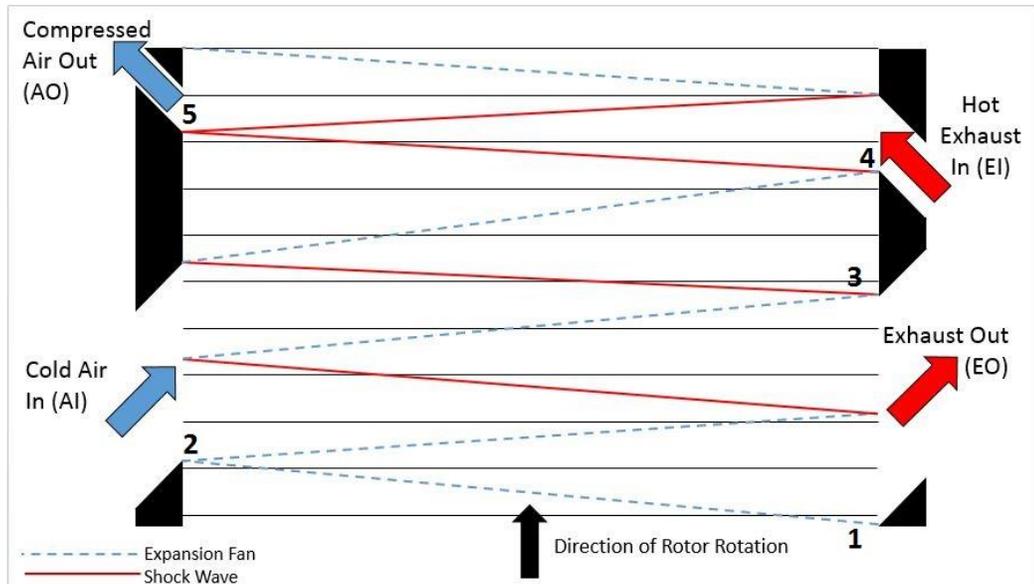
Figure 8: Wave diagram for the compression cycle of a PWS

The overall goal of this process is to introduce high pressure air to the intake manifold with a minimal amount of exhaust gas mixed into the flow. For the Comprex® and the PWS designed in this project, the wave cycle is designed for nine pressure wave reflections. Due to its dependence on the timing of the waves, the performance of the wave rotor is very sensitive to changes from the design point conditions. If the average temperature in the channel or the rotor speed change, the timing of the waves will change. If an expansion fan is allowed to interfere with the main pressure wave due to incorrect wave timing, the performance of the overall cycle will be adversely affected. Because of this extreme sensitivity to the wave timing, a wave rotor will likely not be operating properly during off-design operation. Off-design conditions often result in an increase in the level of exhaust gas mixing. Although some EGR into the intake manifold is beneficial for reducing NO_x emissions and improving efficiency, excessive EGR is undesirable since

24

it yields a severe drop in engine power [3]. Since compression in a PWS is achieved by direct contact between exhaust gases and intake air, a small amount of EGR is generally present, lending to the theoretical ability of the PWS to achieve higher efficiencies, as well as lower NO_x emissions due to the lowering of the combustion chamber temperature.

The length of the rotor corresponds to a certain rotor speed based on the approximate speed of sound in the channel since a pressure wave travels at a Mach number of unity. There should be two cycles occurring for each full revolution of the wave rotor. Since the rotor speed for on design operation of the wave rotor is based on the time it takes for a pressure wave to travel the length of the rotor, operation at speeds other than the design speed results in losses and excessive EGR.

Without some method of improving off-design performance, the range of engine speeds for wave rotor operation is very limited. In order to improve the performance of the PWS at rotor speeds other than the design point, the Brown Boveri Company (BBC) introduced shock wave reflection pockets in the design of their endwalls [4]. The endwalls of the Comprex ® designed by BBC are shown in Figure 9.
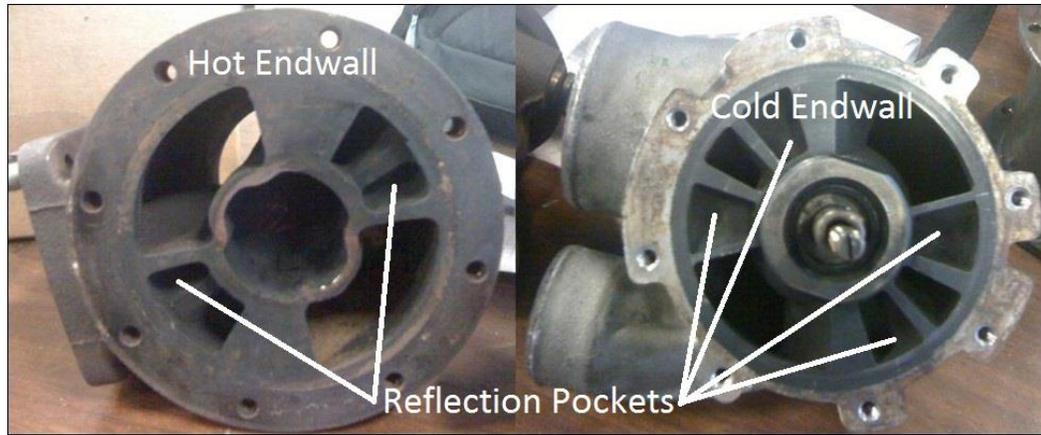
Figure 9: Endwalls of the Comprex® PWS

The four pockets in the cold side endwall correspond to a compression pocket and an expansion pocket for each cycle, while the two pockets in the hot side endwall correspond to one gas pocket per revolution. The compression pocket helps to maintain pre-compression of the intake air for low rotor speeds. The expansion and gas pockets help to maintain scavenging for off-design operation. Without the reflection pockets, off-design operation of a wave rotor will result in poor performance. For this reason, these pockets are crucial for a PWS applied to an engine since the engine and rotor speeds do not remain constant during normal operation of the engine. It is desired to gain a performance advantage from the wave rotor for more than just one engine condition, so rather than just shutting the wave rotor off from the intake and exhaust systems during off-design operation, the pockets provide improved performance over a wider range of engine speeds and load conditions.

II.5 Computational Fluid Dynamics Code

In order to properly design the wave rotor developed in this project, a method was needed to predict the overall performance of the proposed PWS. The method used was a CFD code developed at NASA Glenn Research Center (GRC) by Dr. Dan Paxson et al. [6, 17]. This code has been used by the GRC to simulate the performance of wave rotors that were designed and tested for use as a turbine topping stage. This same code has been used more recently to compare the performance of the Comprex® PWS experimentally against the code's predicted performance, revealing a maximum difference between measured and predicted quantities of 5.96%, and an average difference of 2.77%, as shown by Smith et al. [5].

Other CFD codes have been written in the past to simulate wave rotors [19]. Due to several assumptions, these codes did not yield accurate simulations of the process within the rotor channels. First, these codes assumed an inviscid flow within the channel and a rotor channel that was well sealed at both ends. The codes also simulated the port openings as an instantaneous event, rather than accounting for the time when each end of the channel is moving past the edges of the ports. A proper loss model was also not included that accounted for leakage at the ends of the channel and the volume within the shroud that was not occupied by the rotor. Due to these simplifications, these previous codes resulted in predictions for wave rotor performance that did not closely resemble reality [6].

The CFD code in question is an explicit finite volume technique based on the method of Roe. The code was specifically tailored to wave rotors and assumes the analogy of a shock tube to describe the shock wave compression process as well as the expansion

fan process. The component of velocity in the rotational direction is assumed to be negligible compared to the velocities of the shocks in the axial direction. The code simulates the conditions of a gas inside of a single axial tube that is instantaneously exposed to pressure reservoirs on either end of the tube at certain time intervals based on the rotational speed of the rotor and the angular position and range of the ports. The gas flow in the tube is assumed to be one-dimensional, adiabatic, inviscid, and calorifically perfect. Due to the application of these assumptions, the equations of Euler can be applied in the calculations for the conditions of the flow [6].

In order to solve the Euler equations, a Lax-Wendroff type TVD scheme is applied. The space in the wave rotor tube is broken up into discrete cells. Conservation of mass, momentum, and energy are then assumed for each cell and the flux of each variable into and out of the cell is calculated by use of the conservation equations. The Lax-Wendroff type of solution allows for a valid solution to be found for the Euler equations for both the differential and integral forms of the discrete conservation equations for all conditions, to include discontinuities such as shock waves. This analysis is therefore necessary for this problem since such discontinuities such as shock waves and expansion waves are present [6, 17].

Because obtaining the exact solution to the equations is so computationally expensive, the code utilizes the method of Roe to approximate these solutions. Paxson [6] demonstrates how approximating the solution using this method results in an answer that is extremely close to the exact solution while allowing for the calculation of higher order solutions with sharp resolution at the near discontinuities observed across the shock waves.

28

The large change in properties over a very short axial distance that occurs across a shock closely resemble that of a discontinuity. Because of this, the code models shock waves as a discontinuity for the sake of simplicity.

Because the scale of the PWS designed in this project is so much smaller than that of other PWS designs, scaling-related losses are more significant than for larger PWS designs due to the increased significance of boundary layers, and the closer tolerances needed to avoid excessive leakage. In order to improve on previous attempts at modeling a wave rotor computationally, Paxson et al. [17] made several assumptions that the previous codes had failed to consider. First, the flow is assumed to be a viscous flow with heat transfer flowing to and from the passages. The NASA GRC code also models the time for the ports opening at either end of the passages to be a finite process as opposed to an instantaneous introduction of pressure and temperature. The code also models flow leakage out of the rotor channel based on the clearance from the rotor to the endwall as a loss term. Finally, the code assumes that the angular velocity of the rotor has a significant effect on the flow compared to the axial velocity. These assumptions resulted in predictions for the performance of the Comprex® that more closely resembled the results from testing that will be discussed later in this paper.

II.6 Other Current Wave Rotor Research

Although the Comprex® was designed and successfully implemented for use on a diesel engine, other PWS designs are currently being developed for other types of engines. With the recent increase in the number and scope of environmental regulations leading to

an effective prohibition of the use of diesel fuel and engines for passenger car use [20], the gasoline engine came to the forefront as the primary mode of transportation for small vehicle engines of 2.0 L or less. Because the original Comprex® PWS was designed for a diesel engine where exhaust gas temperature and engine speed change relatively proportionally, a new generation of PWS is currently being developed by ABB for use on a gasoline engine where exhaust gas temperature and engine speed are far more independent. This gasoline engine PWS carries the trade name Hyprex®, and may have the potential to replace costly two-stage supercharging systems [8]. Swiss auto engineering has produced Pressure Wave Superchargers for small automobile engines that have shown significant advantages in low-end power and torque over that of conventional supercharging systems. With the development of the Hyprex®, many of the problems observed for off-design operation of the Comprex® have been mitigated with higher efficiencies and pressure ratios possible for operation at off-design conditions due to the ability to control the rotor speed independently of the crankshaft speed. The benefits of using a PWS on a gasoline engine as opposed to the use of a two-stage supercharger are primarily apparent in the reduction in complexity of the supercharging system. Reducing the complexity to a single-stage system will reduce the weight and decrease the number of possible points of mechanical failure.

II.7 Implementing a PWS in an Engine

Once the scaled PWS designed in this project is properly tested, the potential exists for the device to be mated to the 95 cc Brison as a functional PWS. Several auxiliary

devices are needed in order for the engine to operate properly. During testing by Doerfler [4] EGR was shown to increase markedly for part load conditions, low engine speed operation (such as idle and startup), and low exhaust gas temperature (EGT) conditions (such as cold starting). To avoid excessive ingestion into the engine of exhaust gases, some method of closing off the PWS from the rest of the system is required during engine operation at the previously mentioned high EGR conditions. One method described by Fried et al. [21] was to incorporate devices called a butterfly valve and a snifter valve. During startup, the butterfly valve is used to close the line between the PWS and the intake manifold since the pressure wave process does not operate correctly for the first few moments after startup. This improper operation would cause enough exhaust gas mixing to smother the engine. A separate snifter valve is opened to provide scavenging air for the engine to operate without supercharging during this cold running stage. Once the exhaust pressure becomes high enough to sustain a pressure wave process, the butterfly valve is opened by a piston or diaphragm subject to the pressure differential between the exhaust line and the supercharge airline. The butterfly valve should be closed during startup, warm up, idling, low part-load operation, and when the rotor is stopped due to damage.

III. Experimental Setup

The primary goal of this research was the design of a scaled down Pressure Wave Supercharger sized for a 95 cc two-stroke Brison engine. A secondary goal was the validation of the CFD code developed by Dr. Dan Paxson of the NASA Glenn Research Center that was used to design the device. The validation or invalidation of the code was to be determined by comparison of results between the simulations of certain operating points of the simulated PWS compared with the results from the testing of the physical PWS at these points. Further validation of the CFD code was also performed by repeating tests of the operating conditions of the Comprex® with higher exhaust gas temperatures achieved compared to the experiments performed by Smith [5]. This section details the steps taken to accomplish the aforementioned goals and the tools utilized along the way to quantify and analyze the results of the experiments performed.

III.1 Scaled Pressure Wave Supercharger Design

In order to determine the proper operating conditions that the scaled PWS would need to be designed for, the engine that the PWS is intended for was used as a starting point for the design. Designing a PWS must start with an analysis of the mass flow that is desired to be supplied to the engine. Operation of the engine at sea level standard (SLS) conditions was used as a baseline for the design. The mass flow of air required by the engine is governed by Equation 1 below.

$$\dot{m} = \rho \cdot \dot{V} \tag{1}$$

The symbol ρ refers to the density (lbm/ft^3) of air, and the symbol $\dot{V}$ refers to the volumetric flow rate (ft^3/s) of the air. The volumetric flow rate for the engine was determined using Equation 2.

$$\dot{V} = \frac{N \cdot D \cdot \eta_v}{60} \tag{2}$$

In Equation 2, N is the crankshaft speed of the engine (rpm), D is the displacement of the engine (ft^3), and η_v is the volumetric efficiency of the engine defined as mass of air entering the cylinder at the bottom of its intake stroke compared to the mass of air that would be present for the given volume if the air was of standard density at SLS conditions. For the purpose of keeping the analysis relatively simple, the volumetric efficiency was assumed to have a value of unity. The reference engine condition considered for this project was a crankshaft speed of 7,000 rpm. This was chosen based on the engine speed for the expected operation at altitude for a typical UAV mission. The value for the volumetric flow rate resulting from Equation 2 was calculated to be 0.391 ft^3/s. This value represents the theoretical flow required for the naturally aspirated engine. The mass flow for the engine was then calculated from Equation 1 using standard density, and was found to be 1.76 lbm/min. To account for the increase in flow resulting from using a boosting device, the boosted mass flow was calculated from Equation 3.

$$\dot{m}_{boosted} = 1.5 \cdot \dot{m}_{N/A} \tag{3}$$

The value for the correction factor of 1.5 to calculate the value for the boosted mass flow was based on a rough estimate of the performance gains that could realistically be expected for a turbo-normalization device [10]. The resulting boosted mass flow was calculated to be 2.64 lbm/min. This was the desired mass flow used to design the PWS for the Brison.

The first step in the design of the PWS was to size the air outlet (AO) ports. According to Gyarmathy (12), the area of the AO port (A_{AO}) should account for approximately 10% of the entire area of the rotor face according to Equation 4.

$$A_{AO} = 0.10 \cdot \pi \cdot r^2 \tag{4}$$

Since the compression cycle was to occur twice per revolution for this design, the area of a single AO port was found by dividing the total theoretical volumetric flow rate for the boosted engine by two and dividing it by the inlet flow velocity (u) according to Equation 5.

$$A_{AO} = \frac{0.5 \cdot \dot{V}}{u} \tag{5}$$

The area of one AO port was found to be 0.13 in^2. Equation 4 was then re-arranged to find the radius (r) of the whole rotor. This radius was found to be approximately 0.64 in, although this was not the final exact value chosen. In order to account for any flow blockage in the channel due to boundary layer effects, a Blasius flow profile was assumed according to Equation 6.

$$\delta^* = \frac{1.72 \cdot x}{\sqrt{Re_x}} \qquad (6)$$

Re_x is the Reynolds number with respect to the distance from the entrance to the channel (x). δ^* is the displacement thickness of the velocity profile. This theoretical flow blockage was used to apply a correction to Equations 4 and 5. Another iteration of calculations was performed and final rotor dimensions were chosen based on the results. Table 1 shows the chosen final values for the rotor based on the calculations described above, with some values being determined with the help of the on-design simulation that will be discussed in Section III.2.

Table 1: Final physical dimensions of the rotor

Chosen Rotor Parameters:		
$r_o =$	0.813	in
$r_i =$	0.531	in
$r_o/r_i =$	0.654	
$D_o =$	1.625	in
$L =$	1.600	in
$h =$	0.281	in
$w_i =$	0.108	in
$w_o =$	0.181	in
$w_{avg} =$	0.145	in
$A_c =$	0.041	in^2
$D_h =$	0.216	in

Next, the design speed of the rotor was determined based on the rotor length. The design of this wave rotor is a two cycle-per-revolution design. Each compression cycle results in the shock wave traversing the total length of the rotor nine times [6]. Therefore, one full revolution of the rotor should occur in exactly the same amount of time for a shock wave to traverse the length of the rotor eighteen times. Assuming an average temperature

of 790 R inside the channel, the speed of sound (a) was calculated to be approximately 1,380 ft/s according to Equation 7 below.

$$a = \sqrt{\gamma \cdot R \cdot T} \qquad (7)$$

The ratio of specific heats (γ) was assumed to be 1.4, and the standard value for the ideal gas constant (R) of 1,716 ft*lbf/slug*$^\circ$R was used. The time (t_s) for a pressure wave to traverse the length of the rotor (L) one time was then calculated using Equation 8.

$$t_s = \frac{a}{L} \qquad (8)$$

The total time (T_s) for one full revolution of the rotor and the rotor's angular speed (ω, rpm) were then calculated using Equations 9 and 10 respectively.

$$T_s = t_s \cdot 18 \qquad (9)$$

$$\omega = \frac{60}{T_s} \qquad (10)$$

Based on these equations, the angular velocity of the rotor (ω) for the conditions corresponding to on-design operation was found to be 34,500 rpm.

III.2 Scaled Pressure Wave Supercharger Design Point Simulation

The parameters calculated in the process described above were collected into a spreadsheet and used to determine the inputs for the CFD code in order to model the rotor. The PWS designed for this project was extremely similar in geometry and function to that

the of Comprex®, so it was assumed that the port opening angles found as a result of the research done on the Comprex® would provide the best tradeoff between functionality and time invested for the design of the scaled PWS. The CFD code calculated the conditions within the rotor channels by use of the Navier-Stokes equations [6]. The results can be interpreted via a MATLAB script written by Paxson [6] for the express purpose of creating x-t diagrams for pressure and temperature. These diagrams use a color scheme to denote the local pressure and temperature ratios at each location along the axis of the channel for each time step during a full compression cycle. These values are determined by the ratios of absolute pressure and temperature as compared to a reference value. For the simulations performed here, the assumed reference conditions for temperature and pressure were considered to be values of 520 R and 14.7 psia respectively. Since the NASA GRC code only calculates the ratios for the temperature and pressure, the reference condition is arbitrary and will depend on the test case that the simulation is being compared to. The reference condition for a test case would depend on the measured values of the temperature and pressures in the AI line. The x-t diagrams for one cycle of the scaled PWS for on-design operation are included in Figure 10.
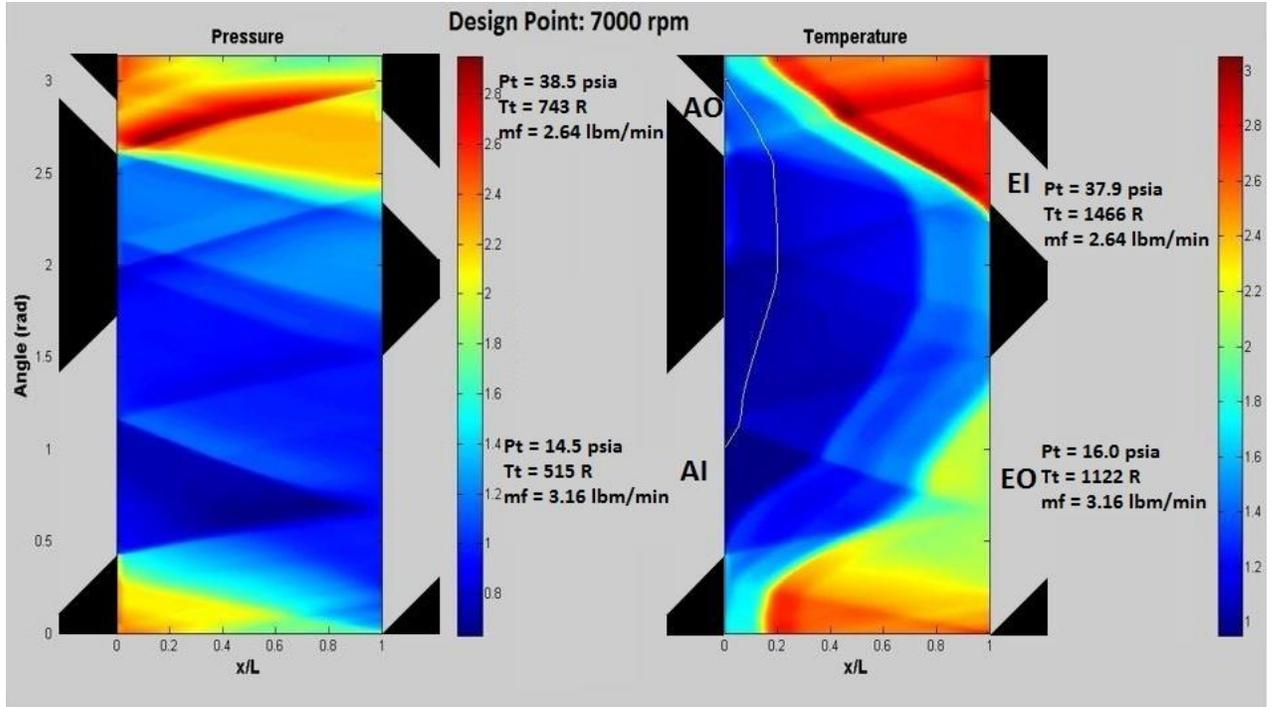
Figure 10: x-t Diagram for the design point of the scaled PWS

The vertical axis in the x-t diagrams is measured in radians, with the end of a single compression cycle occurring at π radians. This results in two full cycles for a full revolution of 2π radians. The diagrams are oriented in such a manner that the cold endwall interface occurs at x/L=0, and the hot endwall interface occurs at x/L=1. In order to better demonstrate the significance of Figure 10, the port opening angles are included in Table 2 below.

Table 2: Port opening and closing angles for the scaled PWS

	Port	Opening Angle (rad/deg)	Closing Angle (rad/deg)
x/L = 0	AI	0.419/24	1.728/99
	AO	2.531/145	2.845/163
x/L = 1	EO	0.000/0	1.501/86
	EI	2.234/128	2.781/159

The port opening and closing angles show that the results of the simulation correspond to air being forced out of the AO port at high pressure and relatively low temperature. The goal of any turbo-normalization device is to increase the pressure of the intake charge air with minimal temperature gain so as to increase the density of the air as much as possible according to ideal gas behavior. The exact results of the simulation for the on-design performance of the scaled PWS are included in a table of the CFD code's output in Table 3 below. Once again, the reference temperature and pressure were 551 R and 14.7 psia respectively, with the mass flow derived from the CFD code's calculation of the corrected mass flow.

Table 3: On-design simulation results

Port	$\dot{m}$ (lbm/min)	π	τ
AI	3.156	0.990	0.991
AO	2.640	2.622	1.428
EI	2.640	2.580	2.820
EO	3.161	1.092	2.157

In Table 3, the important results from the CFD code are given in terms of the mass flow, pressure ratio, and temperature ratio at each respective port. Instead of calculating the pressures and temperatures at every port, the code calculates the pressure and temperature ratios with all parameters calculated according to their values relative to an arbitrary reference condition. All parameters in the input file were set to their known values for the expected operating conditions at the design point. For example, the pressure and temperature ratios of the air entering the AI port were set to values close to 1.0. The

pressure ratios at the EO port was also set to 1.0 since it expands to atmosphere at the exit of the exhaust, but the temperature ratio was guessed to be closer to 2.0. The temperature ratio at the EI port was based on the exhaust gas temperatures measured by Husaboe et al. [2] for the Brison engine at the design condition of 7,000 rpm. The temperature ratio at the AO port was calculated by the code based on the heat of compression for the AO port's predicted pressure ratio and the simulated level of EGR for the AO outflow.

While the pressures at AI and EO are known, the pressures at AO and EI change based on the operating condition since they are directly coupled. That is, any air mass exiting the rotor through the AO port will return to the rotor through the EI port on the other side after it is mixed with fuel and combusted in the cylinder. Because of this, the pressures at these two locations are variables for the user to change. The operating point of the rotor was found by setting the angular velocity to the design speed and changing the values for P_{AO} and P_{EI} in the code input until the values for the mass flux (MF in the output) balanced. Different values of P_{AO} and P_{EI} can yield multiple operating points, so the mass flow rate through the AO port had to match the mass flow rate that the device was designed for. In order to determine the mass flow from the mass flux calculated by the code, Equations 11 and 12 were used.

$$\dot{m}_{AI} = \frac{0.99 \cdot \dot{m}_c \cdot P_{ref} \cdot A_{AI} \cdot \left[1 - \left(\frac{t}{w_{avg}}\right)\right]}{\sqrt{\frac{R \cdot T_{ref}}{g_c}}} \tag{11}$$

The term containing the web thickness (t) and the average cell width (w_{avg}) accounts for the flow blockage caused by the webbing of the cells. The corrected mass flow rate is calculated by the code. The remaining mass flows were calculated by their mass flux ratios as compared to the AI port. By finding the operating point of the wave rotor where the mass fluxes were balanced at the AO port and the EI port and the mass flow through these ports was simultaneously equal to the mass flow that the rotor was designed for (2.64 lbm/min), the true design point of the wave rotor was found. As an added measure of assurance that this operating point will result in proper operation of the PWS, the mass flows at the AI and EO ports should be higher than that at the AO and EI ports in order to provide excess scavenging air to ensure that there is little to no mixing of the AO air and the exhaust gasses in the channel. In the simulation discussed above this was the case, indicating that the operating point simulated represents realistic conditions that would be viable for improving the engine's performance.

For the first few rotor designs, the required mass flow of air could not be achieved while maintaining the desirable conditions as described above. The code was primarily used to verify the viability of the design derived from the process described in Section III.1. The cell height primarily affects the overall area of the cell's cross section. The final cell height was modified several times based on the output from the code in order to increase the mass flow that the design was able to provide. The rotor was designed for a 24 cell arrangement. The cell width is important for determining the strength of the primary pressure wave. As the cell width gets wider, the strength of the primary shock generally decreases [22]. The number of cells also determined the average width of each cell. The

final cell width was chosen due to its ability to meet the performance requirements of the wave rotor designed in this project as simulated by the code that were primarily driven by the mass flow requirements of the Brison engine.

Due to the code's usefulness in allowing a visualization of the processes that occur within the rotor channels, the code was instrumental in driving the design of the rotor by showing that the initial designs could not meet the optimal requirements. For the first few design iterations, the cell height (and by extension the overall rotor volume) had to be increased in order to determine a realistic design that accounted for probable losses that would supply sufficient mass flow of air to the engine while maintaining enough excess air to avoid excessive EGR.

III.3 CAD Design of Rotor and Supporting Parts

After the rotor and relevant device parameters had been properly designed and simulated to demonstrate the viability of the theoretical device as a supercharger, the supporting parts had to be designed to account for the desired parameters. Although much of the ideas regarding physical packaging were borrowed from the Comprex®, some of the parameters for the scaled design had to change to incorporate the differences in the designs.

The Comprex® was designed for a rotor angular velocity of approximately 15,000 rpm for proper operation at its design point. Due to the much smaller physical size of the scaled PWS, the design speed for the scaled rotor was close to 35,000 rpm. This increase in speed is due to the fact that the angular velocity of the rotor is directly related to the time

it takes for a shock wave will take to traverse the length of the rotor. For the scaled PWS, the rotor length was selected to be 1.600 inches based on the calculations performed during the design process (section III.1). The rotor length was a design choice in order to keep the radius to length ratio (0.508) as close as possible to that of the Comprex® (0.592) while keeping the length relatively long to keep the rotor speed as low as possible. Due to the overall reduced size of the scaled rotor, its length is much shorter than the 3.54 inches of the Comprex®. The geometry of the rotor cells was driven in part by a desire to maintain a hub-to-tip ratio of as close to 0.7 as possible in order to avoid a large disparity in the flow profile at each port from the inner radius to the outer radius. The final design had a hub-to-tip ratio of 0.65. The CAD model for the final rotor design is depicted in Figure 11.
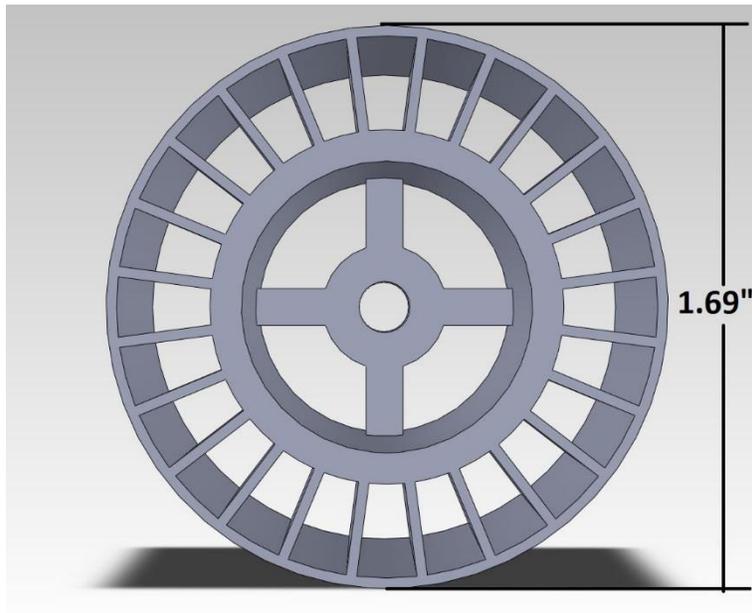

Figure 11: CAD model of final rotor design

43

For the test rig, the Comprex® was driven by a belt connected to a motor in order to control the speed. The speed of the rotor was measured by use of an optical sensor that was excited by a speck of reflective tape on the pulley wheel attached to the rotor. For the much higher speeds of the scaled PWS, a belt system was undesirable due to its high bending moment on the end of the shaft, the potential for heat generation due to belt slippage, and the potential for belt failure. A direct drive system was selected with a brushless electric motor and compatible Electronic Speed Controller (ESC). The motor selected was a Vented Ballistic 550 4.5T electric motor with a Pulse Brushless Pro Racing ESC, as shown in Figure 12.

Figure 12: Brushless motor (L) and ESC (R) for driving the scaled rotor

In order to properly direct the flow of air and exhaust gases, the internal geometry of the cold endwall and hot endwall respectively had to be relatively complex. Although the device would initially be used for testing exclusively, the endwalls were designed to be small with the position of the device relative to the engine in mind so that the overall device could feasibly be mated with the Brison 95 cc engine and carried by the small aircraft that

it was intended for. The ports were designed to angle the flow coming into and out of the rotor at 45 degrees with respect to the axis of the rotor, so the ports had to be angled accordingly. The cold and hot endwalls are shown in Figure 13 and Figure 14, respectively.
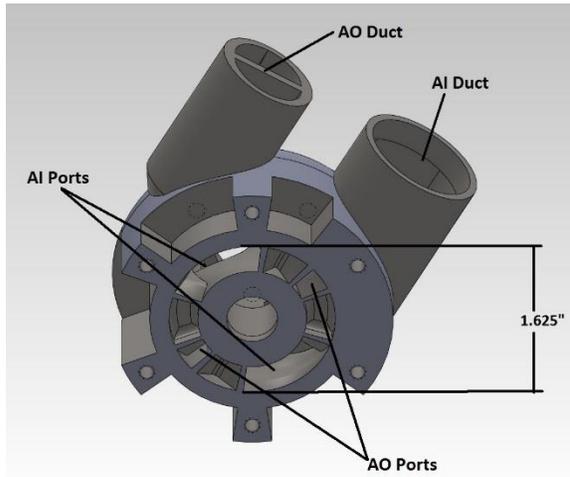
Figure 13: CAD model of cold endwall
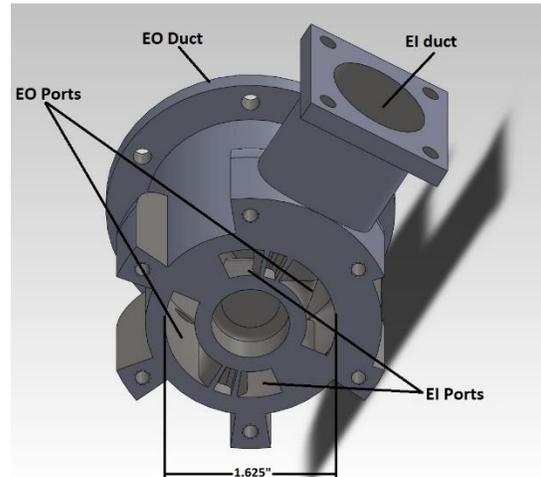
Figure 14: CAD model of hot endwall

The noticeable gaps about the outer edge of the device are regions of material that have been removed for the purpose of reducing the weight of the overall device. The endwalls were also designed with endwall pockets in order to diminish itinerant shock waves and expansion fans to improve the off-design operation of the device. The addition of these pockets mirrors the Comprex® design that was modified based on observations by BBC that the pockets were necessary to avoid heavy EGR and low efficiencies during off-design operation [4]. Without these pockets, the off-design performance of the PWS would be diminished due to shock waves and expansion fans reaching each respective end of the channels at the wrong moments in time. Since the timing of the waves within the channels would be incorrect, compression and expansion of the gasses within the channel

would occur at inappropriate times, causing the performance of the overall cycle to diminish. This could result in severely diminished pressure ratios at the AO port, or possible excessive ingestion of exhaust gasses by the engine due to an increase in mixing between the air and exhaust at the AO port. The NASA GRC code does have a limited capability to simulate these pockets and they were simulated in the CFD work described in section III.2. The code also has a limited capability to eliminate the pockets in order to demonstrate the effects of removing the pockets on off-design operation of the PWS. In order to see the effects of removing the endwall pockets, simulations were performed with the pockets effectively removed by reducing their leakage volume in the code's input file. Unsurprisingly, removing the pockets did not have a major effect on wave rotor performance at the design point. However, for running the rotor off-design there was an observed significant increase in the temperature ratio. The results of these simulations will be discussed in further detail in section IV.2.

Along with the endwalls and the rotor, a rotor shroud, shaft, and a system to properly support the rotor were devised. Much like the Comprex® design, the scaled PWS rotor will be cantilevered via a shaft mounted in the cold side endwall. Shielded ball bearings will be used to support the shaft to ensure minimum friction and a resistance to thrust load to ensure the location of the rotor during operation. Since the rotor shroud is designed for a clearance from the rotor face to the endwall of 0.005 in., the shaft had to be constrained in its longitudinal motion as well as keeping the rotor concentric to the device. The CAD assembly for the physical design is depicted in Figure 15.

Figure 15: CAD assembly for final PWS design

III.4 Test Rig Design

A similar test bench to that developed by Smith et al. [5] is currently being built to simulate the operating conditions of the scaled rotor. Figure 16 depicts the flow path for the four primary air ports to the wave rotor. The test rig designed for the scaled down PWS was similar to the Smith et al. [5] design for testing the Comprex® with the notable exception of the drive system. A brushless electric motor and speed controller will be directly coupled to the rotor shaft using a Lovejoy coupling to drive the rotor into the speed range from around 25,000 rpm up to 34,500 rpm. Controlling the speed of the motor enables matching of the rotor speed for different operating conditions, thus avoiding excessive EGR.
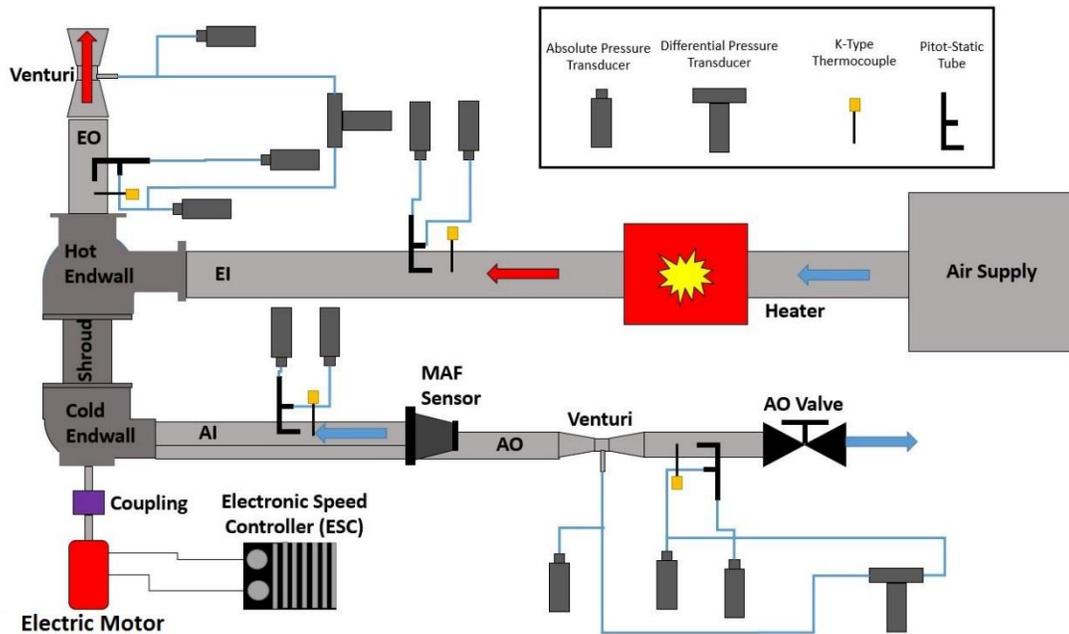
Figure 16: Schematic for scaled test rig design

As shown in Figure 16, the facility heater heats the EI line from ambient temperature to the desired temperature. With the lower mass flows required for this wave rotor, it is anticipated that higher inlet temperatures will be achieved due to an increased ability to heat soak the air before it is supplied to the rig. The heater elements are capable of achieving a maximum temperature, limited by the sheathing, of up to 1660 R. The maximum temperatures observed in the air supply tanks were approximately 1160 R at a mass flow rate out of the tank of 13.1 lbm/min. Since the scaled wave rotor will draw a maximum mass flow rate of around 3.0 lbm/min, it is expected that the supply air should be able to reach a higher temperature during testing of the scaled device.

Mass flow into the AI pipe will be measured directly using a mass airflow (MAF) sensor, similar to the method used to determine the intake mass flow for most engines. Measurements of pressure and temperature will also be taken for the air exiting the AO pipe to measure the mass flow of air actually being provided to the theoretical engine. A valve at the end of the AO pipe will be used to simulate the backpressure in the AO line. This backpressure would be present if the pipe led to the intake manifold of the Brison engine instead of the open end of a pipe. The venturis for the new setup were also designed to be smaller than the large rig for each respective line in order to ensure that the pressure drop across the venturis would be large enough to be read by the transducers. The AO venturi was designed for a mass flow of 2.6 lbm/min (the design point) with the ability to measure mass flow from approximately 1.0 lbm/min up to 5.0 lbm/min. The EO venturi was also designed for measuring mass flow near the design point of 3.0 lbm/min and a range of approximately 1.0-5.0 lbm/min. Accessory heaters will be added to the line leading to the EI port in order to add heat and enable the user to control the temperature closer to the EI port with a faster response time than for the main heater. These heaters are small resistance heaters that wrap around the outer diameter of the pipe. The heaters are supplied with power from a power strip connected to a standard 120V power source.

In order to further validate the CFD code, simulations of the scaled PWS will be compared to experimental data gathered using the test rig in a similar process to that described for comparing simulated performance of the Comprex® to the measured performance. Conditions relating to the engine's expected boosted performance such as exhaust gas mass flow and temperature will be used to simulate a test point. The test bench

with the scaled PWS will then be used to run an actual test of those conditions in order to compare predicted performance with actual performance. This data is very useful for verifying whether or not the CFD code accurately predicts the performance for small-scale version of the PWS, as well as for determining the behavior of the PWS when subject to a range of realistic operating conditions. The test conditions desired to be tested for the scaled rotor and their logical development, as well as the test data gathered from the Comprex® testing will be further discussed throughout Chapter IV.

III.5 Mass flow, pressure and temperature measurements

In order to ensure that the PWS was being properly tested, the conditions in the piping leading to each port had to be measured. While the temperature and pressures for each port are clearly important, the mass flows are equally as important since they need to be properly balanced at each port in order to mimic the mass flow balance for the PWS when affixed to a real engine.

In order to measure the pressure of the flow exiting/entering each port, bungs were incorporated into the design of the endwalls in order to mount 1/16 in. pipe fittings for thermocouples and pitot tubes. These probes were used to measure the total and static pressure in each pipe. The total and static ports of the pitot-static tube were connected to an Omegadyne PX-219, 60 psi absolute pressure transducer with 1/8 in. inner diameter tygon tubing. This allowed for the pressure transducers to be mounted in a location that was far removed from the actual flow in order to reduce the exposure of the sensors to the high temperatures of the flow being measured. In order to measure the temperature in the

pipe, k-type thermocouples were attached to the pipe using swagelok fittings so that the thermocouple tip would sit near the center of the pipe. This location was selected to get the best possible measurement of temperature without the interference of the boundary layers near the walls of the pipe. This was also the approximate location that the pressure was being measured at, providing two measurements at approximately the same location.

III.6 Venturi Design and Calibration

While pressure and temperature are needed to compare against simulated values, the mass flow at each port are also required to ensure that the PWS is being tested in accordance with realistic conditions. With this in mind, the devices chosen to measure mass flow were venturis made from pieces of tube welded to concentric reducers as depicted in Figure 17. The chosen outer diameters for the venturis were 1 in. inlet to a 0.5 in. throat for the AO venturis, and 2 in. inlet to a 0.75 in. throat for the EO venturi. These values were based on an simple preliminary analysis to determine the proper sizes for venturis that would fit the tubing sizes of the test rig and result in an easily measureable pressure drop. All tubing and reducers had a 0.065 in. wall thickness.

Figure 17: Welded venturis: AO venturi (L) and EO venturi (R)

The venturis measure the pressure drop (ΔP) between the entrance and the throat of the venturi for the flow exiting the AO and EO ports. The mass flow for an incompressible flow can then be calculated by using Equation 12.

$$\dot{m} = \frac{C \cdot A_a \cdot \sqrt{2 \cdot \Delta P \cdot \rho}}{\sqrt{\left(\frac{A_a}{A_b}\right)^2 - 1}} \tag{12}$$

where A_a is the area of the entrance to the venturi and A_b is the area of the throat. The discharge coefficient (C) is determined during the calibration of the venturis that will be discussed later in this section. For the calibration process, a known mass flow supplied by the testing facility is passed through the venturi and C is calculated from the resulting ΔP, the known areas, and the density of the air that is determined by pressure and temperature measurements taken in the tube.

In order to ensure that the mass flow could be measured accurately by the venturis, they had to be calibrated against known mass flows in order to determine the actual discharge coefficient. The venturis were each attached to a pipe with flow supplied from the facility. Known mass flows were then run through the pipe increasing in increments

within the designed mass flow range for the venturi of 0 to 5 lbm/min. The resulting static pressure differential from the throat to the inlet in the venturi was recorded at each increment. The total and static pressures as well as the static temperature were also recorded. The pressure differential data was then used to construct a plot of mass flow versus pressure differential in the venturi, and curve fit equations were generated. The resulting plots from the calibrations of the AO venturi and the EO venturi are shown in Figure 18 and Figure 19, respectively.
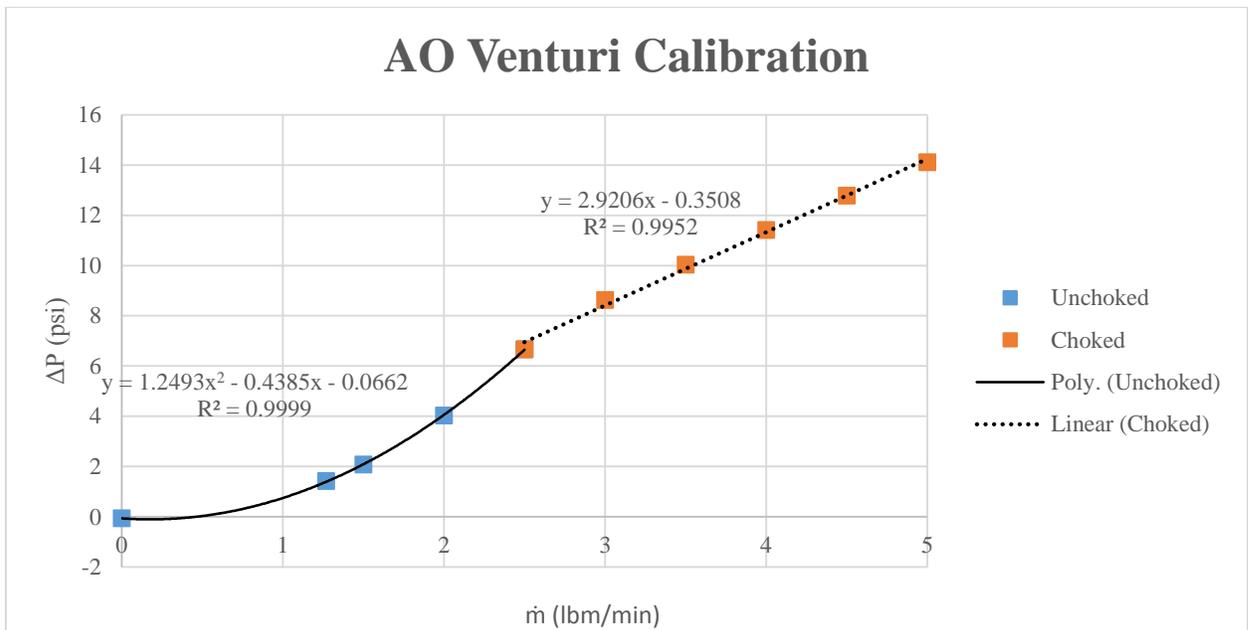
Figure 18: AO venturi calibration curve
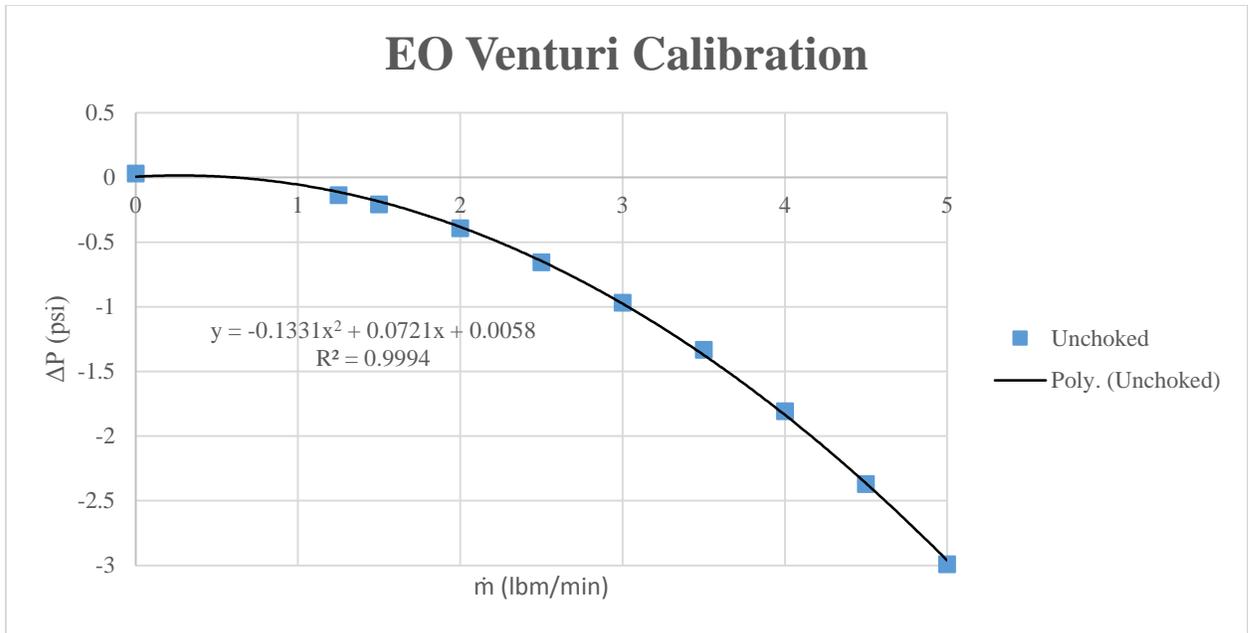
Figure 19: EO venturi calibration curve

For each data set, data was taken for mass flows of 5 lbm/min down to 1.5 lbm/min in 0.5 lbm/min increments, and then for 1.25 lbm/min and 0 lbm/min. The reason data was not taken for 0.5 lbm/min and 1.0 lbm/min was because the nozzle being used to measure the mass flow supplied from the facility unchoked below 1.25 lbm/min. The R^2 value displayed on the plots indicates a very close match between the measured values and the curve fits for all of the data taken. As can be seen in the data for the AO venturi calibration, the flow in the throat of the venturi chokes around 2.5 lbm/min. Because of this, the relationship between mass flow and pressure differential changes from a parabolic to a linear profile at this point.

In order to properly characterize the venturi, the total pressure, static pressure, and temperature were used in combination with the pressure differential and the mass flow in

order to calculate the discharge coefficient. Once the data had been collected, the first step

in this process was to calculate estimated mass flows based on the collected information.

These estimated mass flows would then later be compared to the actual mass flows that are

known from the laboratory's instrumentation in order to calculate the effective area. Since

the effective area is close to the true area at the venturi throat, the effective area was initially

set to the true area. The mass flow estimation for a compressible flow at each data point

was calculated using Equation 13.

$$\dot{m}^2 = 2 \cdot g_c \cdot A_{eff}^2 \cdot \left(\frac{\gamma}{\gamma - 1}\right) \cdot \left(\frac{P_s}{R \cdot T_1}\right) \cdot \left[\left(\frac{P_t}{P_s}\right)^{2/\gamma} - \left(\frac{P_t}{P_s}\right)^{\gamma+1/\gamma}\right] \tag{13}$$

Where T_1 is the static temperature of the flow through the venturi, P_s is the static

pressure at the throat of the venturi, and P_t is the total (in this case stagnation) pressure in

the flow. The effective area is used to define the discharge coefficient as calculated in

Equation 14. The effective area was found as the value that minimized the average error

for all data points between the actual mass flow being supplied to the venturi, and the

predicted mass flow as calculated in Equation 13. In order to find this point, Excel solver

was used by minimizing the sum total of the error values for all the data points taken. The

error for a single data point was found according to Equation 15, as shown below.

$$C = A_{eff}/A \tag{14}$$

$$Error = \frac{\dot{m}_{predicted}}{\dot{m}} - 1 \qquad \text{(15)}$$

This method was used to calculate the discharge coefficient for both the AO venturi and the EO venturi. The discharge coefficient was found to be 0.92 for the AO venturi with an effective area of 0.099 in^2. For the EO venturi, the discharge coefficient was found to be 0.96 with an effective area of 0.289 in^2. These values are both lower than the value of 0.98 that is generally accepted for a venturi designed to measure mass flow. However, the current machined venturis do not exactly conform to ASME precision contractions and expansions. These are hand-made from standard tubing and reducers. Regardless, the current calibrated venturis served the needs of this experiment.

III.7 Further Testing of the Comprex®

Although Smith et al. [5] were able to gather valuable data on the Comprex®, the temperature capability of the test bench at the time had been somewhat limited. Smith et al. [5] was only able to achieve a maximum temperature for the EI port of 883 R. Since typical EGT's for a diesel engine are around 1460 R, the 883 R achieved by the test rig was not sufficient to properly simulate the engine conditions desired. Because of this lack of capability, the mass flows in the Comprex® were never properly balanced during testing according to the proper operation of the device achieved when it is coupled to an engine.

In order to increase the EI temperatures for the test bench, several modifications were made to the test bench itself as well as the facility. First, the main line supplying the hot EI line was insulated. This measure helped to increase the EI temperature to 985 R. However, some of the lines closer to the test bench were still totally uninsulated, so they

were wrapped with fiberglass insulation and small resistance heaters were wrapped around the outside of the tube walls to add more heat to the flow. These modifications enabled a further temperature gain to 1035 R.

With the increase in the EI temperature, new simulations were performed that indicated the possibility to balance the mass flows for the device. These simulations were then compared to experimental data for an operating point that was found to properly balance the mass flows at the appropriate ports. The results of the test and the simulation will be shown later in Chapter IV and discussed in more detail.

IV. Analysis and Results

For this project, four major objectives were undertaken. First, the testing done by Smith et al. [5] was repeated with a modified test facility in an attempt to enhance the temperature capability of the facility to broaden the data collection. Second, this data was used to further validate the CFD code of Paxson [6, 17]. Third, using the NASA GRC quasi 1-dimensional CFD code coupled with mathematical modeling, a scaled down PWS was configured. A subset of this objective was to understand the off-design performance of this scaled down wave rotor. Fourth, this small scale wave rotor was designed using CAD software and manufactured by direct metal laser sintering technology. A test facility was designed in order to evaluate the small-scale PWS that had been designed. The data resulting from all these objectives will be presented and discussed in the following sections.

IV.1 Testing of Comprex® PWS and Validation of the Paxson CFD code

During their validation of the NASA GRC CFD code, Smith et al. [5] ran multiple test cases for the Comprex® that were representative of realistic engine load conditions. The first set of data gathered was from a test point designed to match Smith et al. [5] test point of the Mazda 2.0D engine running at 2,500 rpm, requiring 13.1 lbm/min into the EI port with a rotor speed of 10,625 rpm. This test was run at an EI temperature of 883 R, the highest temperature possible for the test facility at the time. Modifications to the test facility enabled the same tests to be conducted at an elevated EI temperature of 978 R. A comparison of the results from this elevated temperature test point compared to the old test

point is shown in Figure 20 below, with tests being conducted for varying the rotor speed

and the AO valve position independently of one another.
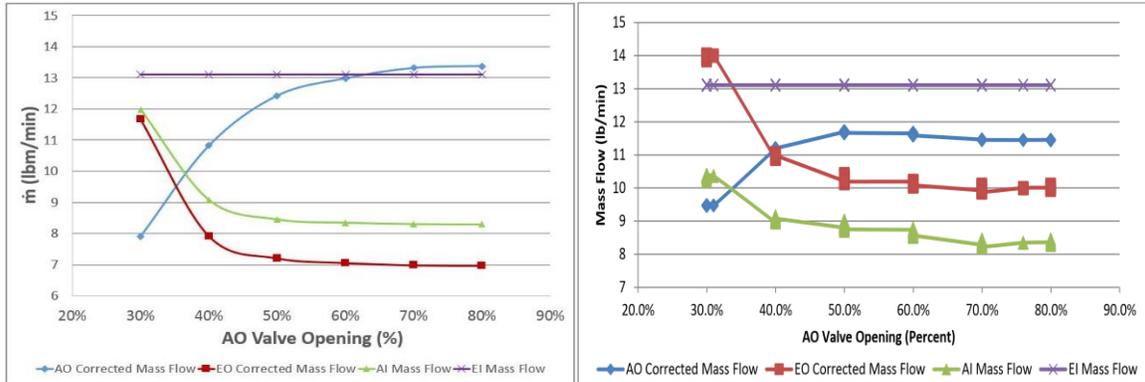
Figure 20: Comprex® data for: modified test rig (L), and old configuration taken by Smith et al. [5] (R)

The plot on the left shows the data taken at elevated temperature. The new data

shows a closer match for the mass flows for the ports that are supposed to be matched (EI

with AO and AI with EO), with the AO mass flow essentially balancing with the EI mass

flow. Although the observed mass flow trend is encouraging, it is interesting to note that

the mass flow for the AO and EI ports are still much higher than the mass flow through the

AI and EO ports. This operating condition would result in a high level of EGR since less

mass is entering through the AI port than is entering the intake manifold through the AO

port. This means that the excess mass flow going into the engine must come from the EI

port. The only thing changing from the left-hand plot to the right-hand plot in Figure 20 is

the EI temperature. This test performed on the modified facility indicates an improved

ability of the Comprex® to properly balance the mass flows on the test rig as the EI

temperature increases. This behavior had previously been predicted by Smith et al. [5], who had performed a CFD calculation to demonstrate the ability of the code to balance mass flows at the tested EI temperature, and an elevated EI temperature of 988 R as shown in Figure 21 and Figure 22 respectively.
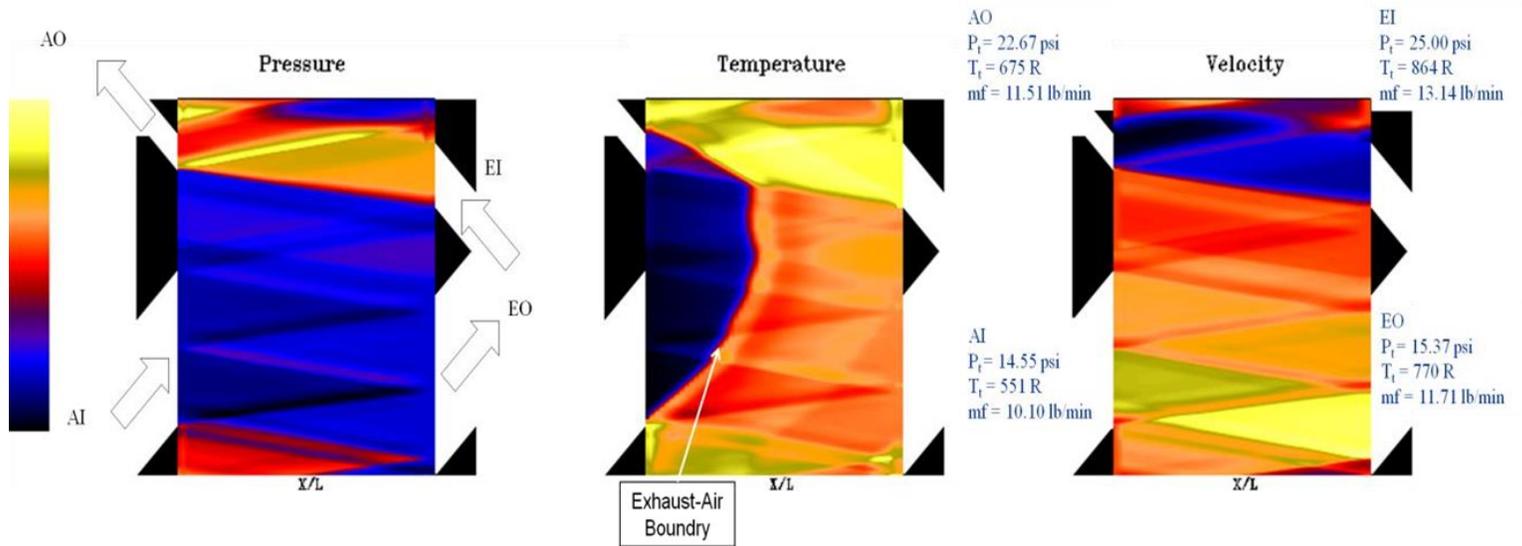
Figure 21:Smith et al.'s [5] prediction for Comprex® performance at tested EI temperature
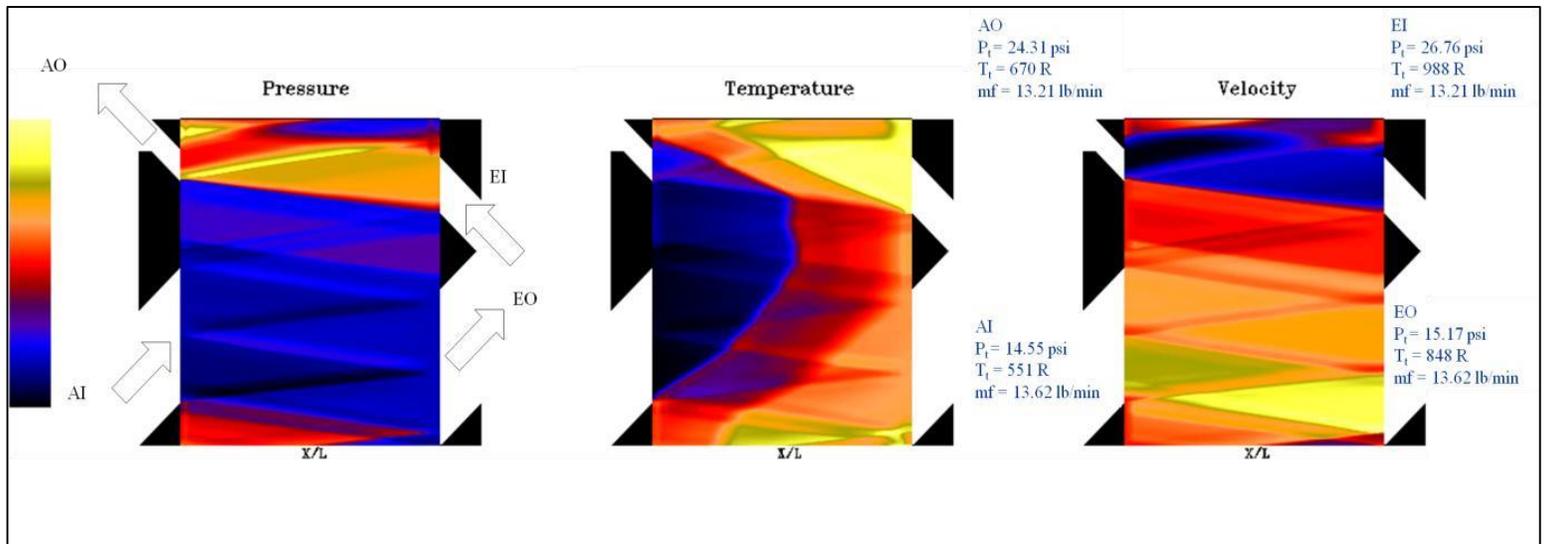
Figure 22: Smith et al's [5] prediction for Comprex® performance at elevated EI temperature

As shown in Figure 22, the elevated EI temperature simulates a more favorable pressure gradient at the EO port, enabling more exhaust gas to be drawn out of the EO port and more air to be drawn into the AI port. Since the rotor speed is not changing between to the two simulations, the wave structure does not change much. With the new elevated temperature capability of the test rig, it was possible to test at the EI conditions of the elevated temperature simulation. In order to validate the simulation, a valve sweep was performed with the rotor spinning at 12,960 rpm as simulated in Figure 22 in order to see if the prediction of the code would match up to an operating point of the Comprex® on the test rig. However, the mass flows did not quite match up as expected for this rotor speed as shown in Figure 23 below. This indicates that the Comprex® was at a slightly different

operating point during the test than the one simulated by Smith et al. [5] shown in Figure 22.
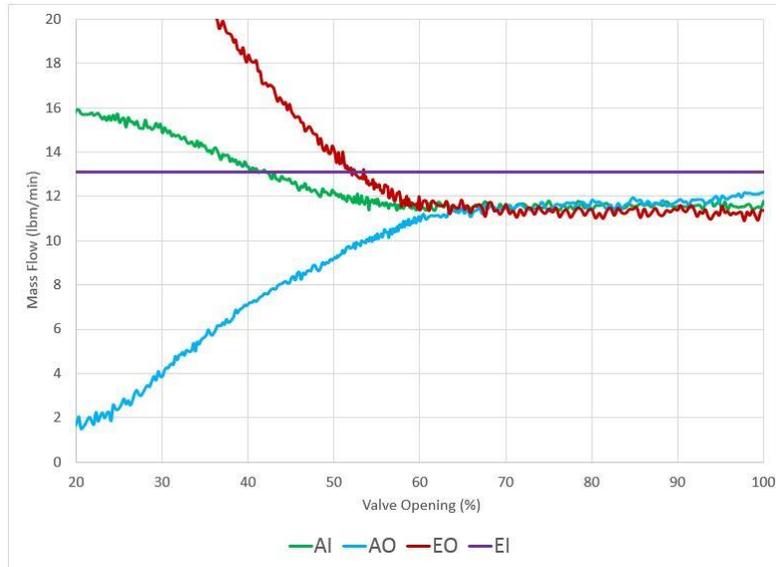
Figure 23: Test point to match conditions of simulation in Figure 18

Although this test point did not yield a balance of the mass flows, the elevated temperatures were found to bring the mass flows closer to balancing. In an attempt to better match the mass flows, more tests were conducted at other rotor speeds. As the speed increased, the mass flows came closer and closer to balancing out. Eventually, a test case was found for a rotor speed of 15,000 rpm where the mass flows were balanced for the 13.1 lbm/min operating condition. The results of the test are included below in Figure 24.
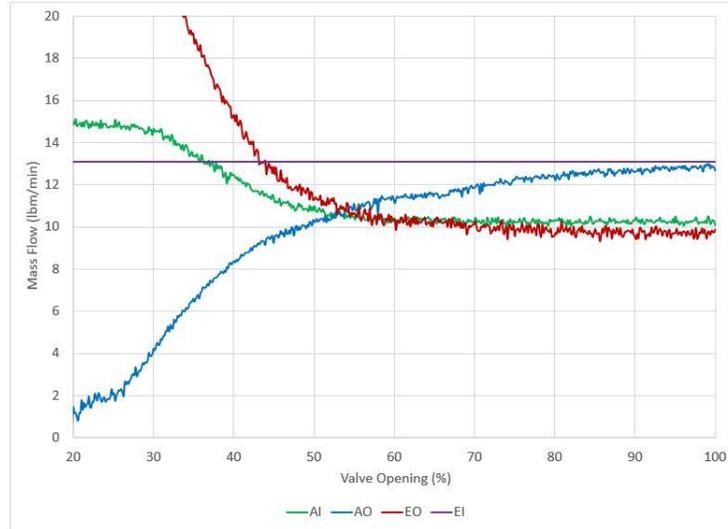
Figure 24: Comprex data point at elevated temperatures with best mass flow matching

For this test point the mass flows balance at the proper ports, although the mass flow is greater for the EI and AO ports than for the AI and EO ports, indicating that the difference in mass flow from that of the AI port to that of the AO port must be made up with EGR for the given operating condition. In order to validate this operating point, the NASA GRC CFD code was used. The results of this simulation are depicted in Table 4 and Figure 25 below.

Table 4: Comparison of experimental and computational results for Comprex® test

	Experimental				Computational				Difference			
	AI	AO	EI	EO	AI	AO	EI	EO	AI	AO	EI	EO
$\dot{m}$ (lbm/min)	10.1	12.95	13.10	9.90	10.14	12.96	12.89	10.08	0.41%	0.04%	-1.61%	1.78%
τ	1.03	1.29	1.97	1.75	1.02	1.34	1.86	1.68	-0.85%	3.77%	-5.57%	-3.85%
π	1	1.25	1.65	1.01	0.99	1.47	1.69	1.05	-1.00%	17.73%	2.21%	3.83%
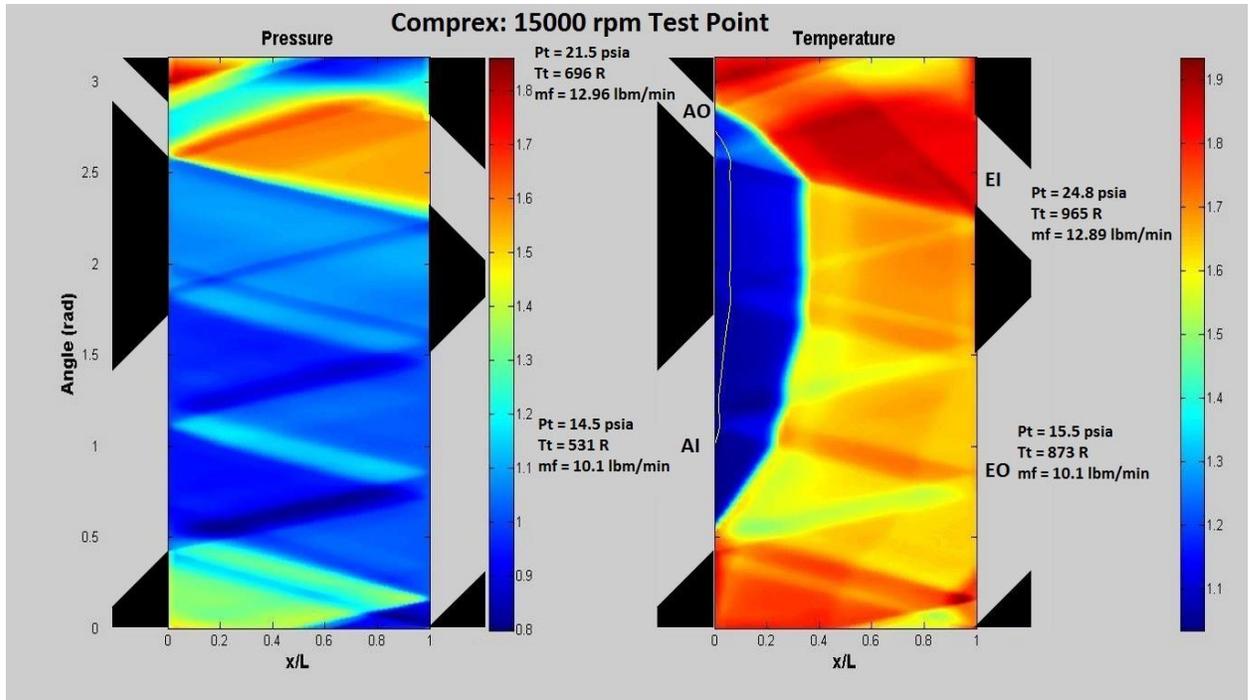
Figure 25: CFD simulation of test point shown in Figure 19

This simulation depicts the operating point for the very end of the test run from Figure 24. This is the point with the most closely matched mass flows for the appropriate ports that has been observed in testing so far. As can be derived from Table 4, the code predicts all values to within 18% of the values observed during testing. If the anomaly of the pressure ratio at the AO port is ignored, the maximum error drops to within 6%. In this case, the EGR evident in the mass flow balance is observable in the x-t diagram, with a sliver of the exhaust gasses being forced into the AO port near the location where the AO port is closed off. The effects of off-design operation are also evident in the x-t diagram, where the slower speed of the pressure wave due to the reduced temperatures causes the primary compression wave to reach the cold side of the rotor after the AO port opens, and the resulting expansion fan that is generated drops the pressure at the AO port considerably.

Since the code calculates the values of the parameters depicted in Table 4 at the rotor face, some of the numbers in the experimental column may not be representative of what the code is calculating. The difference between the calculated and observed pressure at the AO port is most likely due in part to losses from the rotor face to the location where the pressure measurement was taken. All pressure and temperature measurements are taken in the tubing away from the rotor face (downstream for ports with outflow, and upstream for ports with inflow). In the case of the AO and EI ports especially, the ducting from the port to the tubing where the measurement is taken is highly non-linear and very complex in geometry. These factors would contribute to greater levels of loss for the experimental values of AO and EI ports. The measurements with the greatest expected loss are consistent with the error calculated from the CFD code to the experimental measurements as depicted in Table 4, where the greatest error is in fact observed for the AO and EI ports, and it is in the proper direction.

Another source of the error seen here could potentially be due to the way that the code is averaging the values of the parameters at each port. Figure 26 and Figure 27 below show the velocity of the fluid at each respective side of the rotor for all time during the cycle. These figures shows the velocity of the flow at the cold and hot side of the rotor throughout the cycle, with a positive velocity indicating flow into the rotor for the cold side, and out of the rotor on the exhaust side. As shown in the figure, there is variability in the flow from one region of each individual port to another. In the cases of the EO port and the AI port, there are even regions of flow that are moving in the wrong direction. A region of inflow at the AO port is also observable. This non-uniform nature is associated with

operating the rotor far off of its design point, and may also contribute to the code's degraded ability to accurately predict the performance parameters at far off-design conditions. It may be difficult for the code to predict a meaningful average pressure for this flow situation.
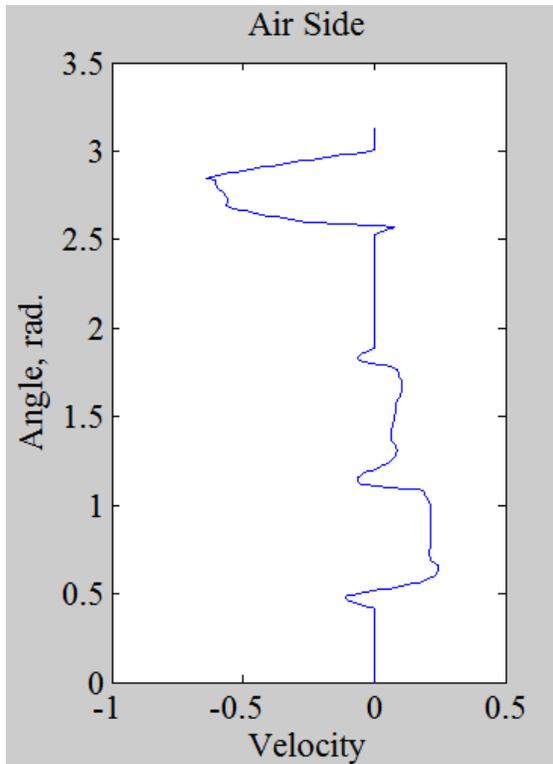
Figure 26: Velocities during simulation at cold (air) end of rotor
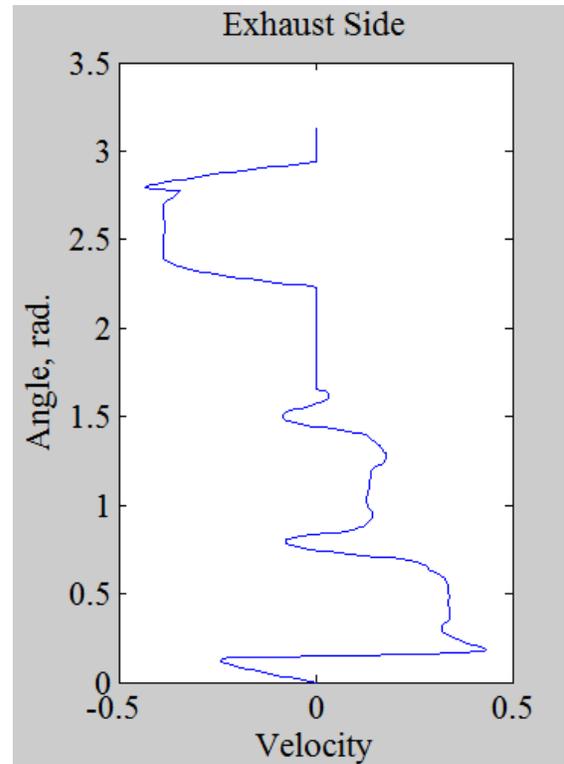
Figure 27: Velocities during simulation at hot (exhaust) end of rotor

IV.2 Simulations for the Scaled PWS

The overall accuracy of the simulations when compared to experimental data was determined to offer sufficient validation of the code's ability to predict wave rotor performance in order to move forward with the project. With this in mind, design work was

performed to determine the proper rotor geometry for the scaled Pressure Wave Supercharger. Once this geometry was determined, the process described in Chapter III was completed. The proper code inputs were calculated from the physical geometry of the wave rotor and simulations of the projected performance of the scaled PWS were performed. These simulations are discussed in further detail in the next section. With the successful validation of the NASA GRC quasi-one dimensional CFD code by Smith et al. [5] and the further validation performed as described in the last section, the design and simulation of the scaled PWS could begin.

Since a wave rotor uses pressure waves to compress air, many of the scaling losses that normally apply to downsizing a compressor do not apply. Since the rotor speed is based on the speed of sound, the speeds reached by a small wave rotor such as the one designed in this project (34,500 rpm) will increase compared to larger rotors such as the Comprex® (15,000 rpm). Most turbochargers for large engines typically spin at speeds upwards of 120,000 rpm [3], with the speeds increasing as smaller compressors are employed for smaller engines. These extreme speeds cause high amounts of friction in the bearings, leading to heat generation as well as inefficient compressor operation. The ability of a PWS to maintain a lower angular speed helps to mitigate some of these losses.

Other losses are amplified for scaling a PWS. For a large scale device where the flow rates are relatively large, the endwall clearance is not as critical for maintaining efficiency since the overall mass fraction of leakage compared to the other flows can still be relatively small for easily attainable clearances. An endwall clearance as small as possible is desired to minimize leakage and thereby maintain as much efficiency as

possible. Once the device is scaled down, the clearance required to maintain the mass fraction of the larger device also decreases. This leads to a much smaller required clearance in order to operate the wave rotor efficiently. Boundary layers will also have a greater effect due to the smaller rotor cells, causing more flow blockage.

Due to the factors discussed above, the losses associated with the small scale PWS are expected to be greater than for the Comprex®. However, the losses of a small scale PWS are expected to be less than that of a small scale turbocharger [7]. For this reason, the validation of the CFD code with the larger Comprex® inspired confidence in its ability to model a smaller scale device properly, including the losses inherent in the device. This design process was described in Chapter III for simulating the on-design operation of the small scale PWS. However, it was also desired to simulate other operating points of the rotor in order to compare its behavior to that of the Comprex®, and to ensure that its off-design operation would be acceptable.

The following sections detail the off-design simulations that were performed in order to analyze the overall performance of the scaled PWS designed in this project. The purpose of evaluating the off-design performance of the scaled PWS is to compare it to the on-design performance. A short discussion of the on-design performance, as well as the x-t diagram and performance table are once again included here for the sake of comparison to the off-design cases detailed in the following sections.

Table 5: On-design performance for the scaled PWS

Port	ṁ (lbm/min)	π	τ
AI	3.156	0.990	0.991
AO	2.640	2.622	1.428
EI	2.640	2.580	2.820
EO	3.161	1.092	2.157
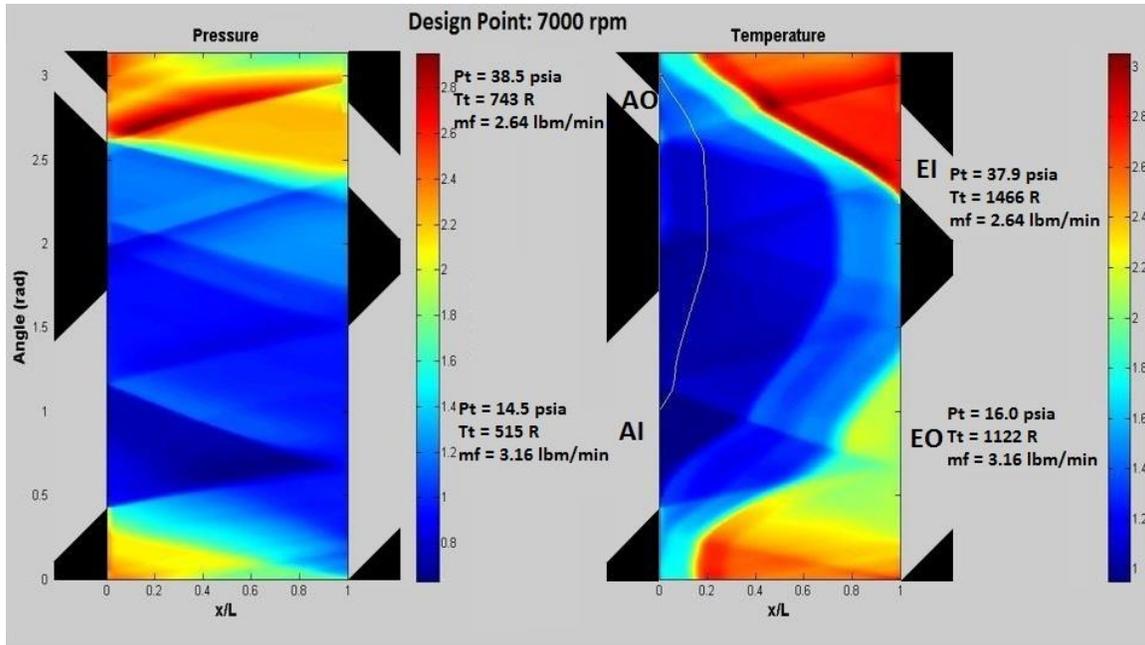
Figure 28: x-t diagram for the design point of the scaled PWS

The scaled Pressure Wave Supercharger detailed in this thesis was designed to boost the performance of the 95 cc Brison engine by 50%, for an engine crankshaft speed of 7,000 RPM. Calculations were performed to determine the boosted mass flow that the engine would demand at this design point at sea level conditions based on the crankshaft speed and the engine's swept volume. The boosted mass flow was calculated to be 2.64 lbm/min. As shown in Table 5 and Figure 28, the final design was simulated for this mass

flow. In order to ensure the proper timing of the pressure waves in the rotor channels with respect to the ports, the rotor speed for the design point was calculated to be 34,500 RPM based on the rotor length and the approximate speed of sound in the rotor channel. The x-t diagram for the on-design case indicates that this rotor speed results in a properly designed wave structure that minimizes itinerant waves and forces the pressure waves to reach the hot and cold ends of the rotor channels at the correct time in the cycle with respect to the port locations. As the boundary conditions are deliberately changed to reflect off-design operation of the scaled PWS in the sections that follow, the overall change in performance of the wave rotor will be discussed.

IV.2.1 CFD Simulations for the Scaled PWS without Endwall Pockets

In order to begin evaluating the small Scale PWS, it was important to begin analyzing its performance for operating conditions beyond that of the design point. As the engine will certainly be operating at speeds other than 7,000 rpm, the rotor speed will also be changing since the rotor will most likely be coupled to the crankshaft for the actual engine. Accordingly, the rotor speed will change as the engine speed changes, causing the engine to demand a different mass flow for each speed. For each different rotor speed the timing for the pressure waves changes, causing the overall wave rotor performance to change significantly. To demonstrate the projected performance of the scaled PWS design, the NASA GRC CFD code was used extensively in order to predict the performance of the rotor at off-design conditions. The resulting simulations are presented and discussed in this section.

As seen for operation of the scaled PWS at the design point (Figure 10 in Chapter III), the pressure waves reflect according to a properly designed device of this type, with the expansion fan from the opening of the EO port reaching the cold side of the rotor just as the AI port opens, and the shock wave from the opening of the EI port reaching the cold side just as the AO port opens. The wave structure is designed to be this way based on the approximate speed of sound in the channel. A more detailed discussion of the designed rotor speed was covered in section III.1 of this paper, with the theory of proper angular port position relative to pressure wave timing covered in section II.4, specifically Figure 8. The speed of the rotor is dependent on engine speed, while the speed of the pressure waves is dependent on EI temperature. The EI temperature is the driving enthalpy behind the compression process and is a function of engine load. Since the engine load can vary greatly for each individual engine speed, the wave structure can be difficult to time correctly as engine speed changes.

In order to demonstrate the effects of changing the engine speed, the PWS in this project was simulated for the on-design speed as well as an off-design speed without endwall pockets. Since the function of the endwall pockets is to get rid of unwanted pressure waves when they occur at inappropriate times, running the rotor off of the design speed should highlight the difference in wave structure well. The code simulates a certain amount of leakage out of each end of the rotor channel as it completes a cycle. In order to simulate the endwall pockets, the code breaks up the leakage volumes into different regions on either end of the channel. For the region where a pocket is present the volume for leakage to occur is increased, thereby representing a pocket. Because of this, the presence

of pockets in either endwall cannot be simulated directly, neither can these pockets be explicitly removed. In order to simulate the pockets, the volume for leakage was increased. For the case of removing these pockets, the volume for leakage to occur was set to a relatively small value.

The first simulation case without endwall pockets was for the design point. Since the rotor speed was designed to accomplish the proper wave structure for ideal operation at the design point, a significant change in rotor performance should not occur by removing the endwall pockets. The primary purpose of the endwall pockets is to modify the wave structure for off-design operation in order to avoid exhaust gas ingestion. With this in mind, the first simulation for on-design operation with no endwall pockets is considered in Figure 29, and Table 6 below. Although there is some observable change in the wave structure, the overall wave structure is preserved and the PWS operates properly. The removal of the endwall pockets results in very similar performance at the design point to the same device with the pockets included. In this case, as in the lower rpm case to be discussed below, the excess air is reduced (from 19% to 13% here). This does not seem to affect the overall performance however, with the total pressure, the total temperature, and the mass flow at the AO port remaining virtually unchanged compared to the design point with pockets. This is indicative of a properly designed device, with the overall performance unchanged at the design point regardless of the inclusion or removal of the endwall pockets.

Table 6: Results for on-design simulation without endwall pockets

Port	ṁ (lbm/min)	π	τ
AI	2.990	0.990	0.992
AO	2.638	2.693	1.437
EI	2.643	2.665	2.820
EO	2.990	1.081	2.213
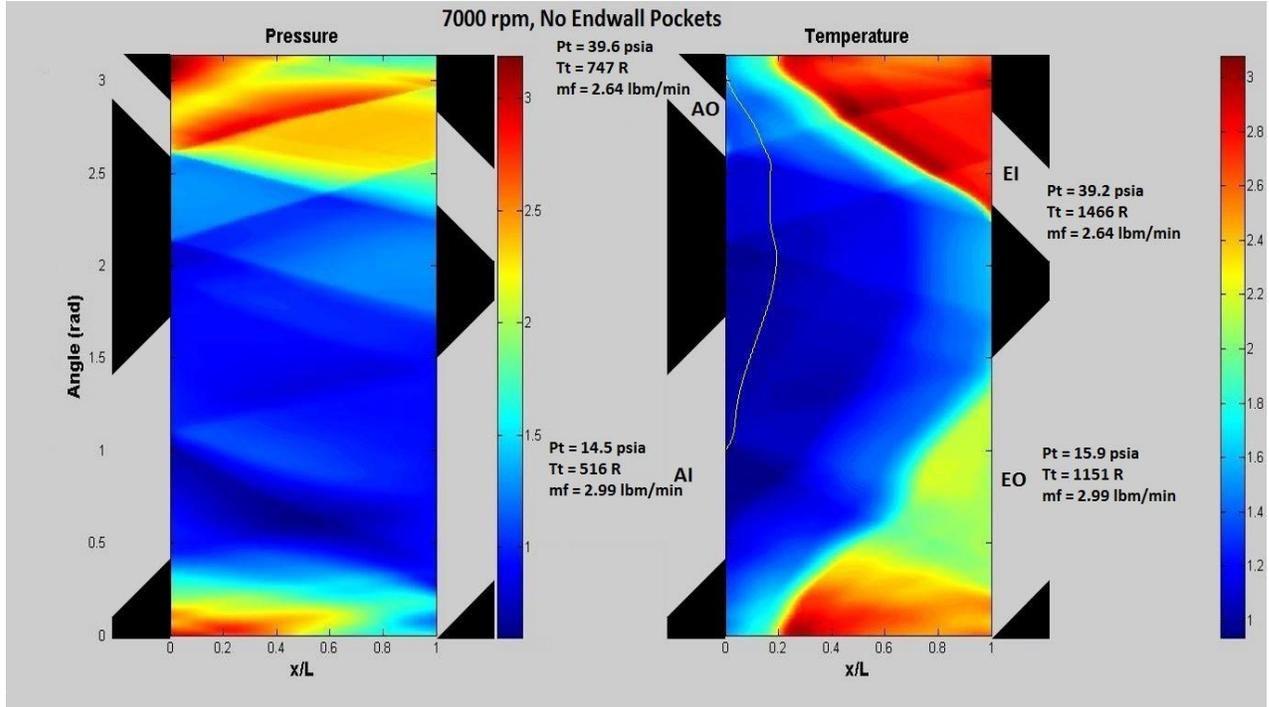
Figure 29: x-t diagram for the design point of the scaled PWS without endwall pockets

In order to fully appreciate the effect of removing the endwalls, an off-design point was also chosen for simulation with no endwall pockets. A simulation for a rotor speed corresponding to an engine speed of 5,000 rpm was modified to remove the endwalls in order to see their effects on the wave structure and the temperature ratio. Once again, a small value for the endwall leakage volume in the region where the pockets are present on

the real device was chosen and a simulation was performed. The results of the 5,000 rpm

case with no endwall pockets are shown in Figure 30 and Table 7 below.

Table 7: Results for the 5,000 RPM simulation without endwall pockets

Port	ṁ (lbm/min)	π	τ
AI	2.182	0.990	0.994
AO	1.890	2.608	1.415
EI	1.893	2.400	2.829
EO	2.179	1.050	2.231
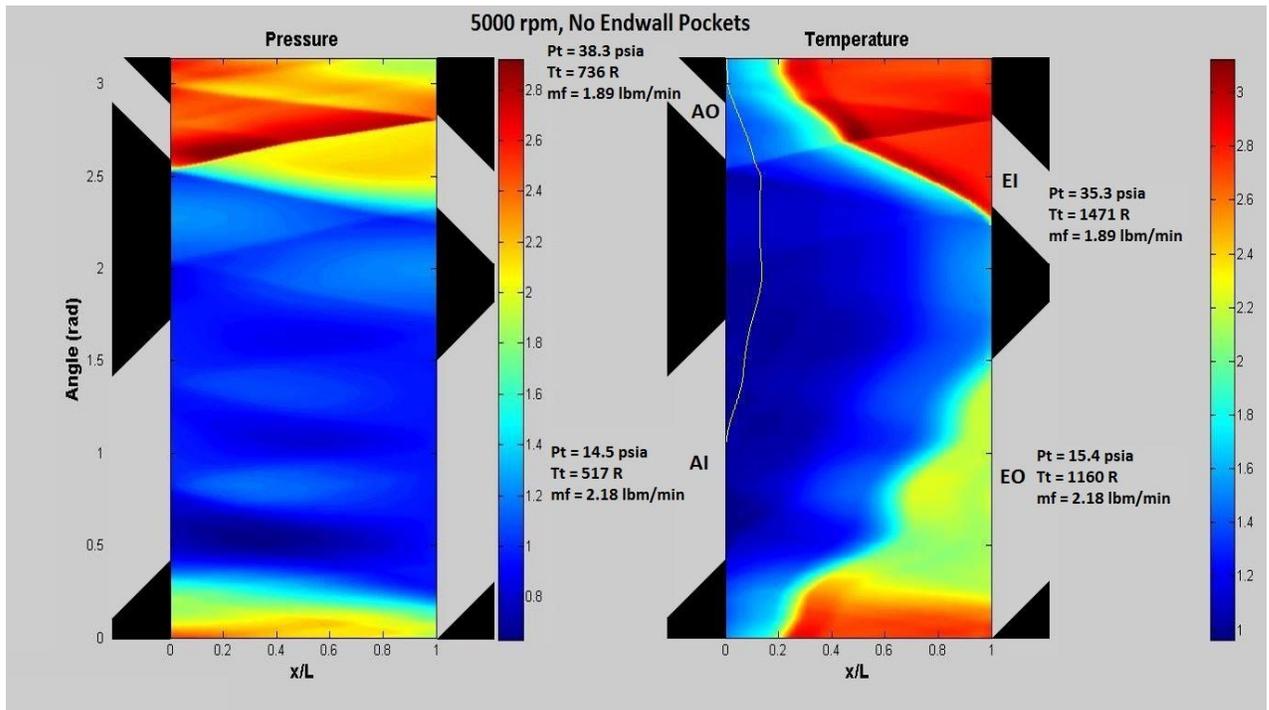
Figure 30: x-t diagram for 5,000 RPM operation of the scaled PWS without endwall pockets

As seen in the figure, the shock reflections are more pronounced in the region where

the pockets used to be as compared to the region between the AI and EO ports where they

are much more prominent for the same simulation with the endwall pockets included as discussed later in this section. Another observed side-effect is the reduction in the excess air to around 15% as compared to the 18% with the endwalls. While the reduction in the excess air due to the removal of the endwall pockets had little to no effect on the temperature ratio for the design speed simulations, the 5000 rpm case shows the temperature ratio jumping from 1.393 to 1.415 at the AO port, and the pressure ratio increasing from 2.332 to 2.608 for comparing performance with and without endwall pockets. Both the total temperature and total temperature were increased in order to maintain the same mass flow rate, indicating lower efficiency. The increase in temperature is reflective of an increase in exhaust gas mixing within the channel, consistent with the reduction in excess air. This increase in mixing for off-design operation without endwall pockets is in line with with the observed poor off-design performance of previous PWS designs without endwall pockets.

Although the removal of the endwall pockets did not show a large effect on AO temperatures, the effect was still observable with a hotter, less dense air intake charge. It is possible that the numbers chosen for the leakage volume were not accurate in representing the design. Without actually testing the scaled rotor, these parameters are difficult to choose accurately in the code and the testing results could indicate that different numbers are more appropriate for the loss model.

IV.2.2 CFD Simulations for the Scaled PWS at Off-Design Rotor Speeds

In order to demonstrate the ability of the final scaled PWS design (including the endwall pockets) to respond to off-design rotor speeds, the code was used to simulate the

device for rotor speeds corresponding to engine speeds of 5,000 rpm, 6,000 rpm, and 8,000 rpm. The simulations indicate that although the wave structure changed for these rotor speeds and engine conditions, the endwall pockets that are included in the CFD code's model were effective in minimizing the negative impact of pressure wave production and reflection at incorrect times within the channels. Without the pockets, the existence of shock waves or expansion fans at certain ports during the cycle due to incorrect timing would seriously degrade the performance of the PWS as demonstrated above. With the pockets included in the model, the simulations for off-design operation were shown to yield favorable pressure ratios and temperature ratios with an acceptable level of excess air.

Initially, a simulation was run for the rotor at an angular velocity of 24,643 rpm. This rotor speed was representative of an engine speed of 5,000 rpm. Since the rotor speed in this simulation was slower than the design speed, the wave structure changed from the design point structure significantly as seen in Figure 31 and Table 8 as compared to Figure 10.

Table 8: Results for the 5,000 RPM simulation

Port	$\dot{m}$ (lbm/min)	π	τ
AI	2.227	0.990	0.992
AO	1.888	2.332	1.393
EI	1.891	2.260	2.829
EO	2.233	1.050	2.190
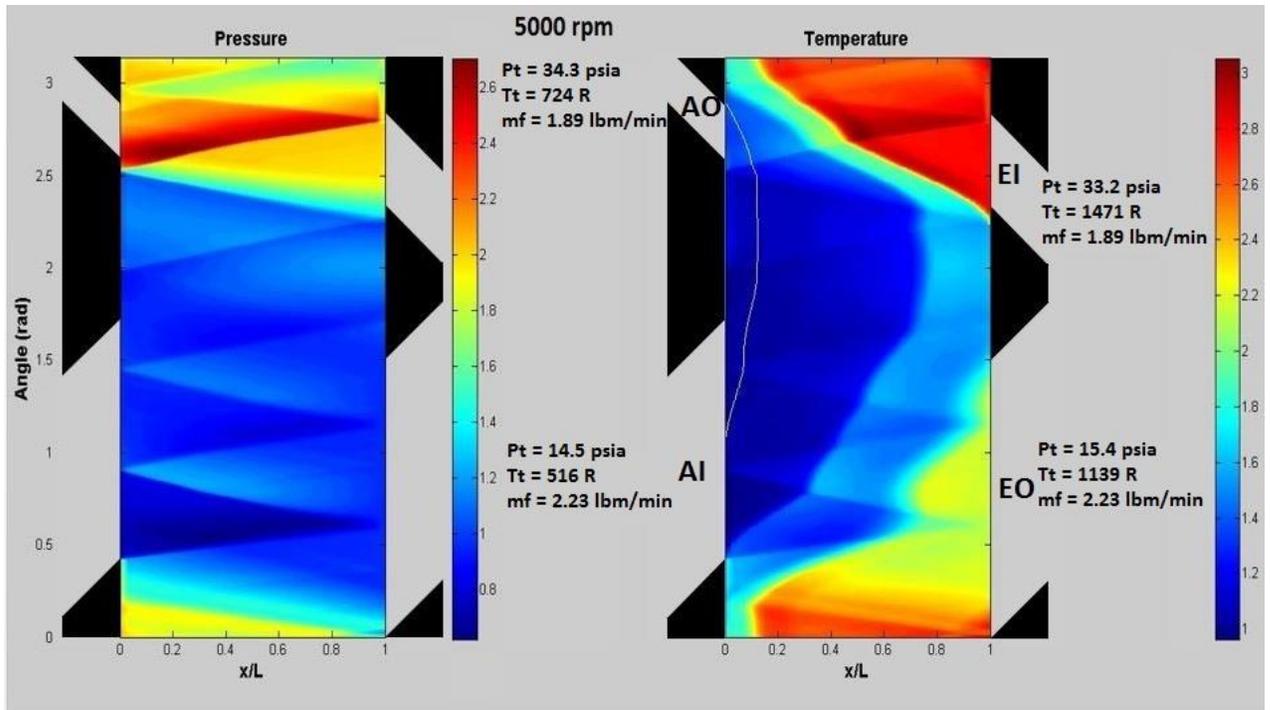
Figure 31: x-t diagram for 5,000 RPM operation of the scaled PWS

As the rotor speed decreases, the wave speed increases relative to the angular velocity so that the pressure waves will reach the opposite end of the channel faster compared to the angular displacement. This leads to a seeming "compression" of the waves as they appear in Figure 31, leading to more than nine pressure wave reflections per cycle. It can also be observed that one of the pressure waves seems to diminish or disappear at an angular position of approximately 1.7 radians. This occurs in the region between the EO port and the EI port where there is an endwall pocket present. This simulation shows that the pocket has done its job in quelling the pressure wave at this location that would have reflected at an inappropriate time relative to the overall compression cycle.

77

As the engine speed changes, an internal combustion engine will demand different amounts of airflow since the intake stroke will occur with a frequency dictated by the crankshaft speed. For this project, the airflow demanded was assumed to be a direct function of the number of intake strokes over time, which is directly related to the crankshaft speed of the engine. The required mass flow for the engine operating at 5,000 rpm was calculated using Equation 3 for the engine operating with 150% volumetric efficiency due a mass flow boost provided by the PWS of 50% over that of a naturally aspirated engine. The simulation predicts that the rotor will be able to provide the required mass flow to the AO port of 1.89 lbm/min. The pressure ratio for the 5,000 rpm case is predicted to be 2.33, boosting the pressure of the air supplied to the engine to about 34 psia. The reference conditions for all simulations performed were a pressure of 14.696 psia, and a temperature of 520 R.

In addition to the 5,000 rpm case, another lowered engine speed test case was simulated for the engine operating at 6,000 rpm. The corresponding rotor speed for this case was 29,571 rpm. The resulting simulation is provided in Figure 32 and Table 9 below. Once again, the perceived "compression" of the pressure waves as compared to the on-design case is observed. The diminishing of the itinerant pressure waves due to the endwall pockets is also observed in order for the compression process to operate correctly, although the effect is not quite as exaggerated as in the 5,000 rpm case. The mass flow required for this case was once again calculated using Equation 3 and accounting for the drop in engine rpm. The simulation predicts that the scaled PWS will be able to supply the required 2.26 lbm/min of engine air with approximately 19% excess air and a pressure ratio of 2.50 and

air pressure in the intake manifold of 37 psia. The temperature ratio for this case was found to be higher than for the on-design case. Since the excess air ratio was largely identical (both around 19%) to the on-design case and the pressure ratio was less, the increase in the temperature ratio illustrates the reduction in efficiency associated with operating the rotor off-design.

Table 9: Results for the 6,000 RPM simulation

| Port	ṁ (lbm/min)	π	τ
AI	2.682	0.990	0.992
AO	2.256	2.498	1.419
EI	2.256	2.400	2.807
EO	2.682	1.075	2.160
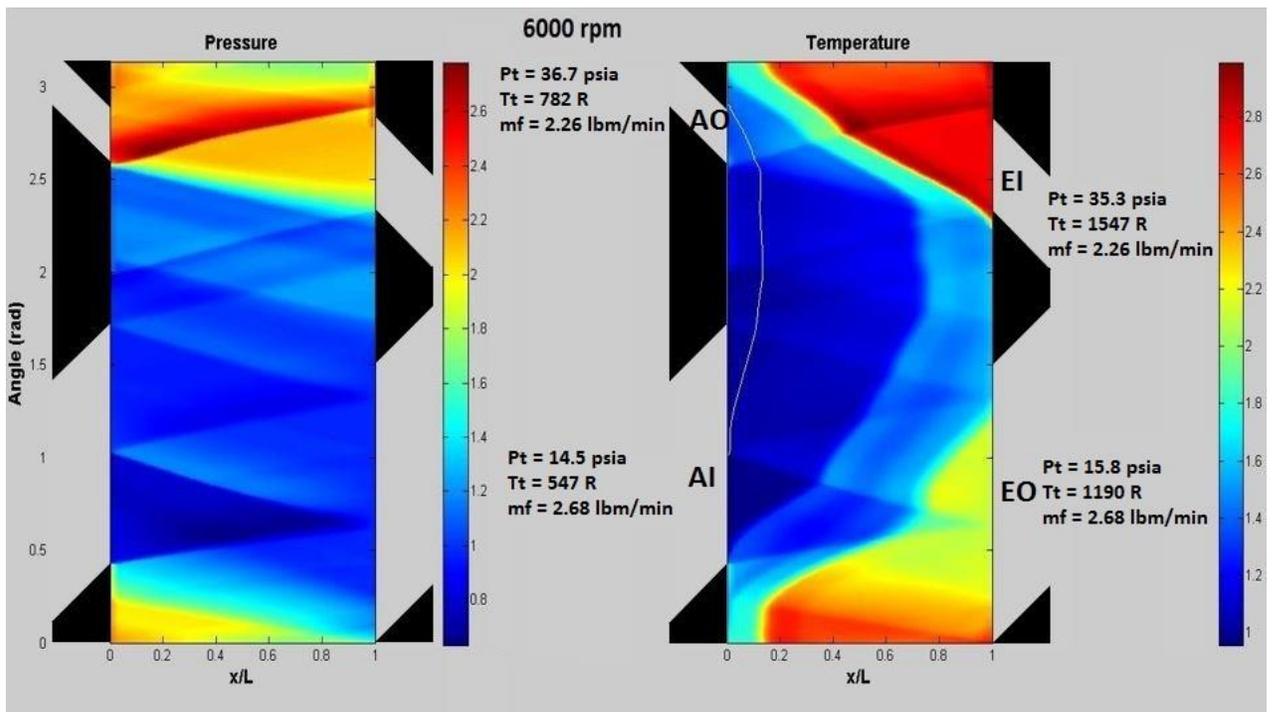
Figure 32: x-t diagram for 6,000 RPM operation of the scaled PWS

For the third off-design case, an engine and rotor speed higher than that of the design point were chosen to simulate. This case was representative of an engine speed of 8,000 rpm and a corresponding rotor speed of 39,428 rpm. The results of the simulation are shown in Figure 33 and Table 10. For the case of a higher rotor rpm than the on-design case, the pressure waves become steeper and more spread out as opposed to the compression of the waves seen in the lower rpm cases. This is because the angular position of the rotor channel will change more as the pressure wave travels from one end of the passage to the other due to the higher angular velocity. Once again, the endwall pockets appear to be doing their job by quelling the unwanted wave reflections, particularly on the hot side around an angular position of 1.7 radians, and the cold side near 2.2 radians before the opening of the AO port.

Table 10: Results for the 8,000 RPM simulation

| Port	ṁ (lbm/min)	π	τ
AI	3.405	0.990	0.989
AO	3.008	2.811	1.496
EI	3.008	2.900	2.958
EO	3.415	1.083	2.268
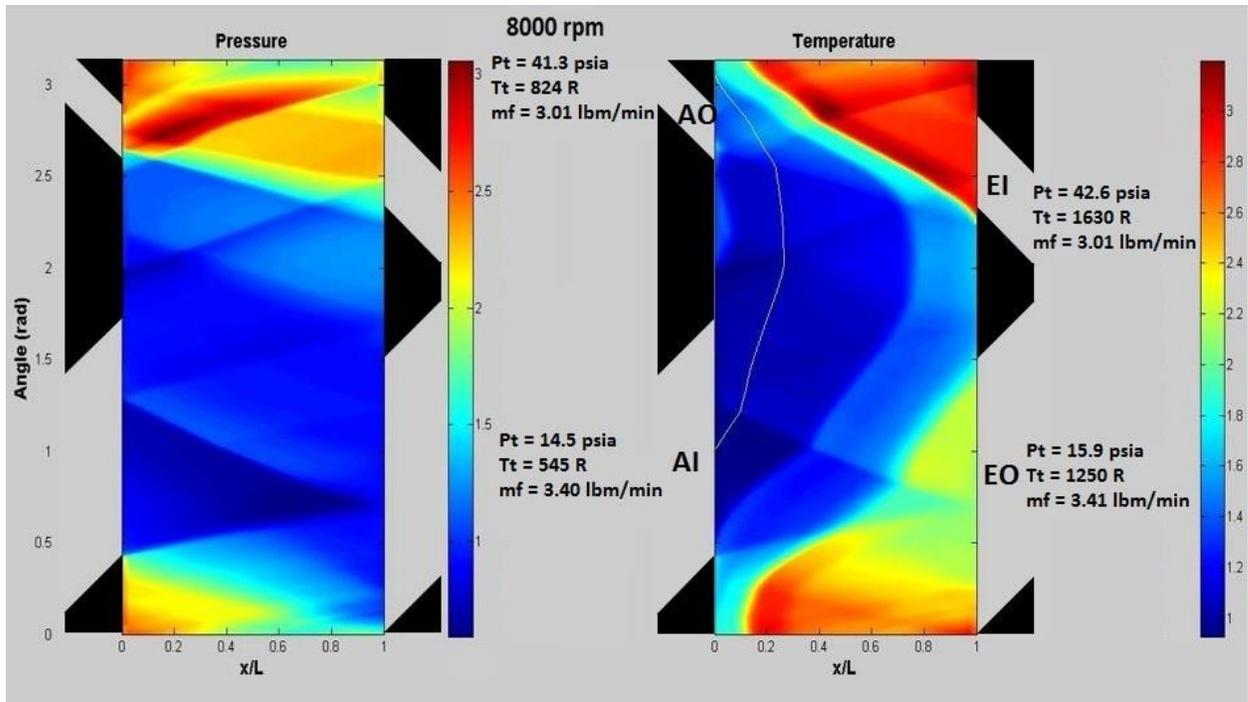
Figure 33: x-t diagram for 8,000 RPM operation of the scaled PWS

The 8,000 rpm simulation predicts that the rotor will be able to provide the required boosted mass flow associated with that engine speed of 3.01 lbm/min with a pressure at the intake manifold of 41 psi corresponding to a pressure ratio of 2.81. However, the temperature ratio is very high at 1.50. This is due to the very high level of compression required for this high mass flow combined with a reduction to about 13% of excess air leading to a probable increase in EGR. The off-design operation again creates a disturbance in the wave structure at the AO port where the primary compression wave is reflected as an expansion fan. This is due to the fact that the pressure wave is not able to reflect off of a hard surface just before the AO port opens as it is supposed to, and instead reaches the cold endwall when the port is open. These effects are predicted to increase the temperature at the intake manifold to around 360 °F. Such high temperatures could potentially lead to

81

engine knock and excessive heating of the engine block if the air temperature is not reduced through the use of an intercooler or some other such device. It is also possible that a different operating point for the rotor could yield a lower temperature ratio that may bring the air temperature to a more reasonable level. This result emphasizes the issue of intake air charge heating when compressing the intake air via direct contact with the hot exhaust gasses.

The three test cases above are representative of the operating range expected for normal use of the engine when installed on the aircraft in question. However, it was also interesting to the designer to explore the behavior of the rotor in situations outside of normal. One case of interest is that of the engine running at a low engine speed such as that of an idling situation. Another abnormal operating point might be how the rotor responds to a relatively cold exhaust temperature such as on engine startup, or perhaps in testing where the high temperatures supplied by a real engine may not be possible to reach for the testing apparatus. For previous Pressure Wave Supercharger designs on larger engines, both of these cases were shown to yield high levels of exhaust gas mixing and generally poor performance. A complex system of spring-loaded valves and tubing to completely close off the PWS from the engine has been devised and implemented on these systems to avoid highly inefficient running, or smothering the engine with too much EGR. Simulations of both of these situations were performed in order to determine whether or not such a complex solution would be required for this application.

IV.2.3 CFD Simulations for the Scaled PWS at Lowered EI Temperatures

The third series of rotor simulations performed was for the case of a lowered exhaust gas temperature at normal operating speeds. This case could be relevant for two different situations. One situation occurs when the engine first starts. During this process the engine block itself has not yet come up to temperature, leading to reduced atomization of fuel droplets and very inefficient combustion. Inefficient combustion leads to a very rich mass air to fuel ratio required to create enough power to run the engine when cold, due primarily to the fact that the engine cylinder and exhaust tubing have not had time to heat up. This adversely affects combustion of the fuel by inhibiting the evaporation of the fuel droplets, leading to incomplete and slower combustion. The lack of heat in the surrounding engine block and cylinder head also simply increases the rate of heat transfer out of the gas to these surrounding walls. These effects combine to provide a relatively low exhaust gas temperature. Without a method of closing off the PWS from the engine, the typical result of these low EI temperatures is very poor performance.

In order to demonstrate the negative effects of reducing the EI temperature, two simulations were performed. The same reference conditions for the AI port of 14.696 psia and 520 R were assumed for the pressure and temperature respectively. The CFD code was then used to demonstrate the change in performance for two low temperature cases.

The first case was for an EI temperature of 1210 R (versus the design EI temperature of 1466 R). It was assumed that this would be the maximum achievable temperature for the test rig equipment currently available. The results of this first simulation are shown in Figure 34 and Table 11. Although less excess air is present (15%

as compared to 19% at the design point with higher temperatures), the code predicts very favorable performance with only a small amount of exhaust gas mixing at the AO port. The code also predicts that the design mass flow of 2.64 lbm/min can be supplied at these conditions. Since the temperature in the channel is lower than at the design point, the wave speed decreases causing the primary compression wave to reach the cold endwall late, resulting in the disturbance at the AO port that has been previously commented on for this condition.

Table 11: Results for the on-design simulation with low EI temperature

| Port	$\dot{m}$ (lbm/min)	π	τ
AI	3.040	0.990	0.992
AO	2.640	2.226	1.348
EI	2.640	2.380	2.302
EO	3.031	1.054	1.843
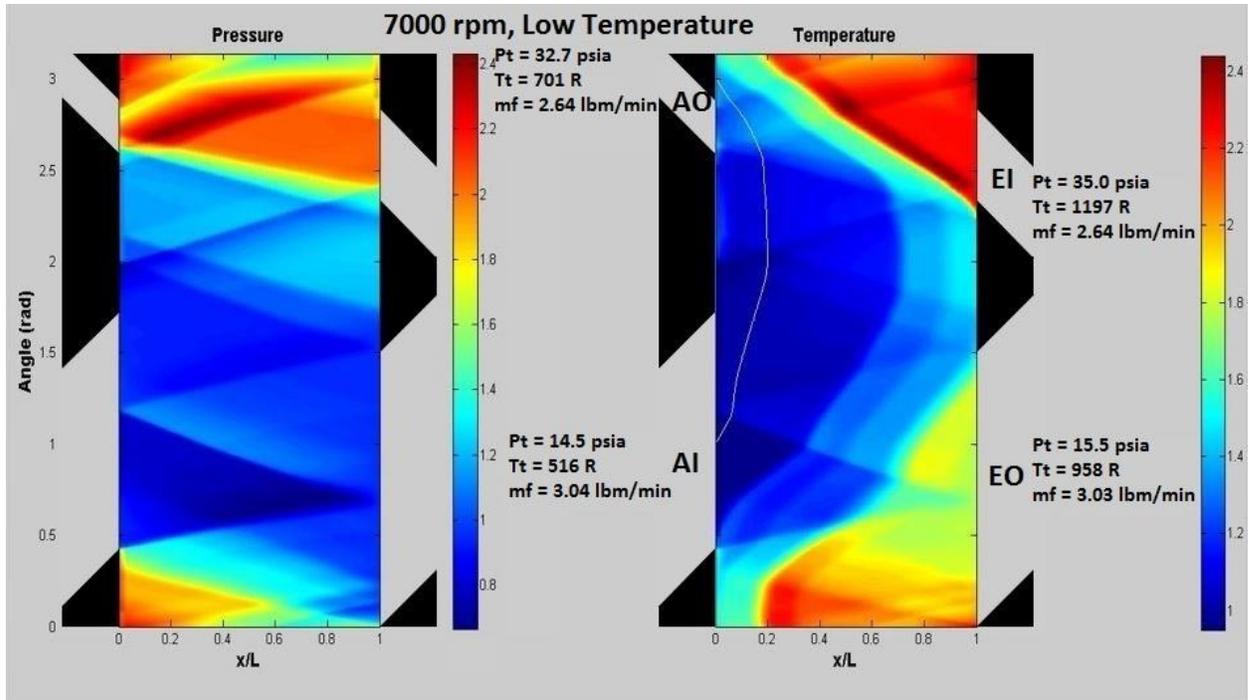
Figure 34: x-t diagram for design point of the scaled PWS with low EI temperature

For the second low temperature case, an EI temperature of 1010 R was tested. The results for the simulation with an EI temperature of 1010 R are depicted in Figure 35 and Table 12 below. This very low temperature case predicts a situation similar to that seen in the testing of the Comprex®. One immediately apparent anomaly is the strange reflection at the AO port that particularly noticeable in the pressure plot. This is once again due to the off-design conditions disrupting the proper timing of the pressure waves, causing the primary compression wave to reach the cold side of the rotor after the AO port has opened. This situation creates a drop in pressure due to the expansion fan generated here followed in quick sucession by a shock wave generated by the closing of the AO port (the blocks in the figure are not perfectly synchronized). Strange pressure wave reflections with inappropriate timing are characteristic of operating a wave rotor far off of its design point.

Since this situation perfectly describes what is being simulated in this case, it is not surprising to see the code showing strange anomalies in the wave structure that are not representative of ideal operating conditions. This operating point would most likely produce conditions similar to that described in the off-design test of the Comprex® from section IV.1, where inappropriate wave timing significantly adversely affects the wave structure leading to the potential for strange variations in the velocity profile. As seen in that example, these conditions could cause reversal of flow for certain ports where such anomalies occur.

Another similarity to the off-design Comprex® case from section IV.1 is the way in which the mass flow is divided for this case. In this circumstance, the mass flow through the AO and EI ports is higher than that through the AI and EO ports. This means that there is a negative value for the excess air entering through the AI port to prevent EGR. This causes a large amount of recirculation of the hot exhaust gasses. This situation also leads to a higher temperature at the AO port due to exhaust gas mixing than would otherwise be present with a buffer region of excess air. Overall, the temperature of the air in the channel is lower than at the design point due to the lowered temperature of the exhaust gas and the lower compression ratios. Although the correct mass flow is supplied to the AO port (and therefore the engine), much of that mass flow is due to the recirculation discussed above. This level of EGR would most likely suffocate the engine.

Table 12: Results for the on-design simulation with very low EI temperature

Port	ṁ (lbm/min)	π	τ
AI	1.903	0.990	0.972
AO	2.659	1.774	1.427
EI	2.659	2.150	1.920
EO	1.908	1.060	1.664
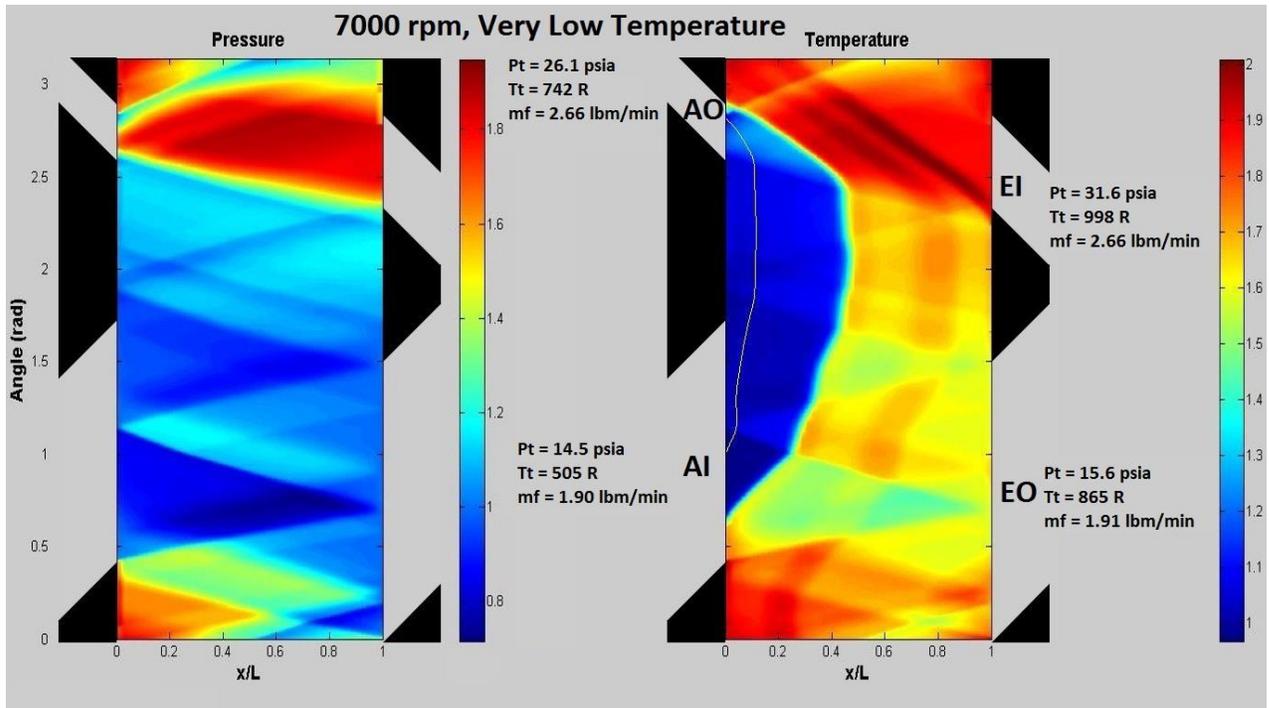
Figure 35: x-t diagram for design point of the scaled PWS with very low EI temperature

IV.2.4 Summary of CFD Simulation Results

For all simulated off-design conditions the code was used to demonstrate the ability of the scaled PWS to provide the mass flow that is demanded by the boosted engine at the relevant crankshaft speed. The simulations performed also indicated certain characteristics of the PWS that were helpful in the overall characterization of the design.

The removal of the endwall pockets showed very little effect on the overall performance for the design point. Since the rotor speed at the design point was selected to minimize the amount of unwanted pressure wave generation and reflection at inappropriate times in the compression process, this result is unsurprising. However, for the 5,000 RPM engine speed case the wave structure showed an increase in the number of itinerant pressure waves that would ordinarily have been removed by the endwall pockets. For the 5,000 RPM case with the endwall pockets included, the pressure ratio was 1.393 as compared to 1.415 with the pockets excluded with the same mass flow. For both cases, the removal of the endwall pockets also reduced the amount of excess air, slightly increasing the temperature ratio at the AO port. The inclusion of the endwall pockets in the final design should help to reduce the number of itinerant reflections and drive the temperature ratio down slightly to help avoid engine knock.

Next, several off-design rotor speeds were simulated. The EI temperature for each case was selected based on dynamometer data taken by Husaboe et al. [2] for the Brison 95 cc engine. For each of the lowered RPM case, the scaled PWS demonstrated an ability to provide sufficient mass flow for the engine at the specified operating condition. The wave structure changed as expected, with more wave reflections at the lower rotor speeds. With the inclusion of the endwall pockets, good performance was achieved for each operating condition with a minimum number of wandering pressure waves that could hinder performance.

As the EI temperature was reduced, the code simulated a tendency for the excess air to be reduced. For the first low temperature case the excess air was reduced, but the

overall performance remained acceptable. The temperature simulated could theoretically be realistic for the actual engine depending on the amount of heat transfer occurring before the exhaust is introduced to the PWS. However, for the very low EI temperature case the excess air became negative. A negative excess air fraction is consistent with all of the operating points that were tested for the Comprex®. During testing, the mass flow for the EI port was held constant. It was observed that as the temperature increased, the mass flow of the AI and EO ports increased. This behavior of the larger PWS is consistent with the predictions produced by the code for the scaled PWS, which would not converge on a balanced operating point for a positive mass fraction at the very low EI temperature.

IV.3 Manufactured Scaled PWS Parts

In order to route the flow into and out of the rotor for a two-cycle-per-revolution design, the internal geometry of the endwalls had to be very complex. This eliminated many conventional manufacturing options such as CNC machining or hand milling. The two most feasible solutions for manufacturing these endwalls were casting and direct-metal laser sintering.

Casting has historically been an extremely common manufacturing technique for parts of complex geometry. The casting process involves the fabrication of a mold and then pouring a liquefied metal into the mold in order to form the part into its desired geometry. Molds can be either permanent or consumable depending on the number of parts required. Since this project required only one copy of each endwall and two copies of the rotor (in case one rotor became damaged), making the molds for the parts would have entailed a

very large cost that most likely would not have been justified given the small number of machine parts required. Due to these factors, it was decided to look for another method of manufacturing the parts.

Another manufacturing method relevant to the complex internal geometry associated with these parts is direct metal laser sintering (DMLS). This method involves building a metal part by addition of a small amount of metal powder on top of the previous layers. Once a very thin layer of powder is deposited, it is melted by a highly focused laser beam. This process requires no mold in order to make the part and the only costs are related to orienting the part properly so that the printer can properly do its job, the cost of the powdered metal, and the post-machining required for areas where close tolerances are necessary. Due to cost constraints, DMLS was selected as the method for manufacturing the major parts of this project to include the rotor and the endwalls.

The first part manufactured using the DMLS process was the rotor. The final rotor that was manufactured is shown in Figure 36. The smooth regions of the rotor on the outer diameter and along the inner diameter of the cells were post-machined due to tolerance and balancing requirements. The outer diameter had to be machined so that it was round and would fit inside the rotor shroud without pieces of material rubbing. The inner diameter was machined to be round and concentric with the outer diameter for balancing purposes. The small diameter hole in the center of the supporting structure for the shaft was also bored so that the rotor could be press fit with the shaft. The only parts of the rotor that were not post-machined were inside of the cells themselves. This region would be very difficult to mill and it would be even more difficult to make all the cells uniform. Since the overall

velocities of the flows moving into and out of the rotor cells are relatively small, fluid friction is not expected to contribute to significant losses within the rotor cell. For these reasons, any attempted post-machining of the rotor cells was deemed unnecessary. In order to reduce the friction without removing an excessive amount of material, the inner surface of the channels may be lightly sanded to deburr the surface.

The scaled PWS in this project was designed to achieve smaller clearances than the Comprex®. Maintaining this clearance is a challenge for a device like this because of the thermal stresses involved. As the individual components change temperature due to the hot exhaust gasses, they expand according to their thermal expansion coefficient. If the rotor experiences a greater heat load than the shroud (which it should), then the rotor will be at a higher temperature and may expand into the shroud. In the case of the scaled PWS, the material selected for the rotor (Inconel 718) has a lower thermal expansion coefficient than the material chosen for the shroud (SS316). This selection was made so that the shroud would expand faster than the rotor, hopefully avoiding impact of the rotor on the endwalls.

Figure 36: Manufactured rotor (Inconel 718)

In order to estimate the difference in thermal expansion that would occur from the rotor shroud to the rotor, calculations were performed based on the material properties. The initial lengths of the rotor and shroud were respectively assumed to be 1.600 in. and 1.610 in. as they were designed. Since the leakage flow is intended to be minimized, it was assumed that the rotor would be heat loaded more than the shroud. Based on a worst-case scenario for operation on the actual engine with EI temperatures approaching 1360 R, the average rotor temperature was assumed to be 1260 R, with an average shroud temperature of 860 R. Based on these conditions, the hot rotor lengths were calculated using Equation 16.

$$L_{hot} = L_{cold} \cdot (1 + \alpha_L \cdot \Delta T) \qquad (16)$$

For the conditions described, the lengths of the hot rotor and shroud were calculated to be 1.608 in. and 1.614 in., respectively. With an initial gap of 0.005 in. at each end of the rotor, these lengths should allow for approximately 0.003 in. of clearance at each side. However, since the rotor is mounted on the shaft on the cold side only, this growth could cause the rotor to clear by less on the hot side than the cold side. If all thermal expansion is assumed to occur with the rotor growing in the direction toward the hot endwall, this worst case scenario still would result in the hot side clearing by 0.001 in. If more clearance were desired on the hot side, it would also be possible to add a shim or gasket between the hot endwall and the shroud. This would allow for more clearance on the hot side of the rotor if necessary.

Because of the complex nature of the internal geometry, the endwalls were also made using the DMLS process. The cold endwall part is depicted in Figure 37. Since the cold endwall was designed to mount the rotor shaft, post machining was performed to the built-in bearing holder inside of the endwall itself. An edge was also built in at the bottom of the holder in order to keep the bearing from moving toward the rotor. The bearing will also be constrained from moving in the opposite direction by an edge built into the shaft design. The rotor face was post machined in order to accommodate the close tolerances necessary between the rotor and the endwall in order to help prevent leakage. The upper face was also post-machined to be parallel to the rotor face so that the upper bearing holder (depicted further down in Figure 39) could hold the bearing and shaft to be perpendicular to the rotor face.
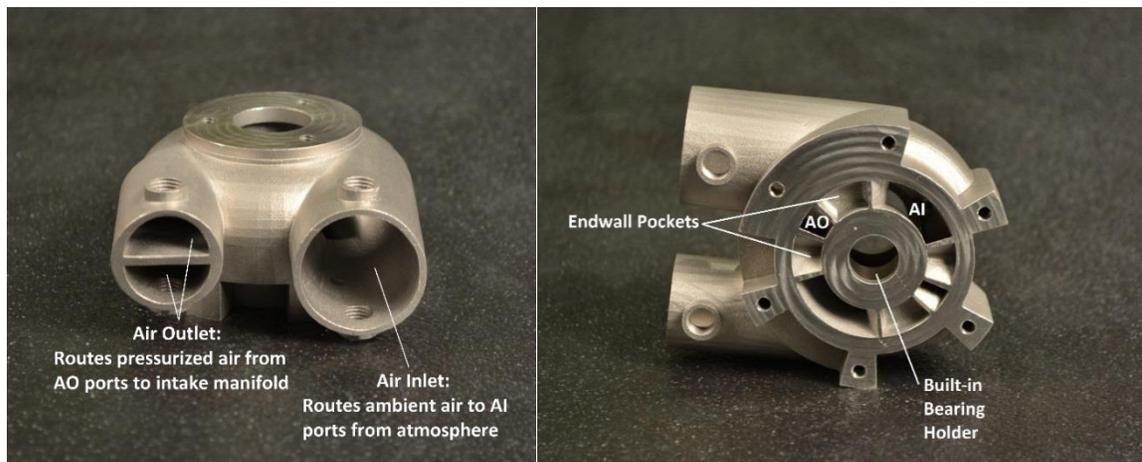

Figure 37: Manufactured cold endwall (Stainless Steel 316)

Much like the cold endwall, the hot endwall was also of complex internal geometry. The hot endwall is shown below in Figure 38. Once again, the rotor face was post-machined to achieve tolerances with rotor clearance. The design for the hot endwall and the cold

93

endwall include bungs for mounting pitot probes and thermocouples. For the Comprex®

tests, it was suspected that losses were not being accounted for due to the locations that the

pressure and temperature of the gasses were measured at. The bungs will enable a better

match of the experimental values to the location that the code calculates them (the rotor

face). In order to measure these values as close to the location that the code was calculating

them (the rotor face) as possible, bungs were incorporated into the design. As with most

turbochargers, it is desirable to include a wastegate into the system in order to control the

charging pressure. A system very similar to that of the Comprex® will be used in this

design, with a flat disc valve that may be controlled by the mounting lever that runs through

the side of the endwall. The hole for the valve allows the exhaust gas to exit from the EI

ducting to the EO ducting as seen in the figure.
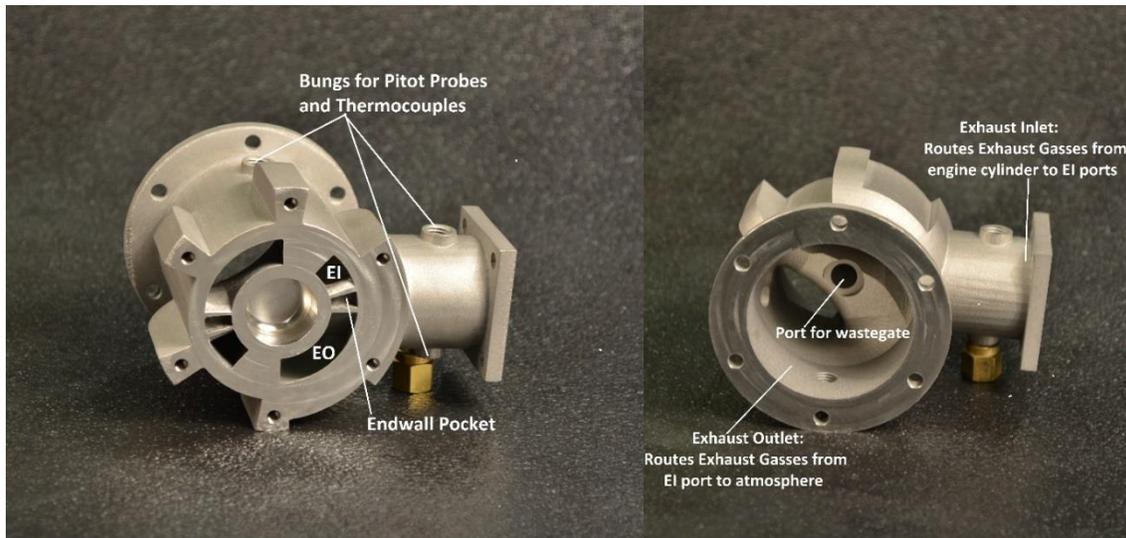
Figure 38: Manufactured hot endwall (Stainless Steel 316)

The manufactured parts were assembled in a manner similar to the exploded assembly view from the CAD program as shown in Chapter III. A picture of the final parts in this orientation is shown in Figure 39 below. The parts will be assembled according to this configuration and integrated into the small scale test rig that will be completed shortly.
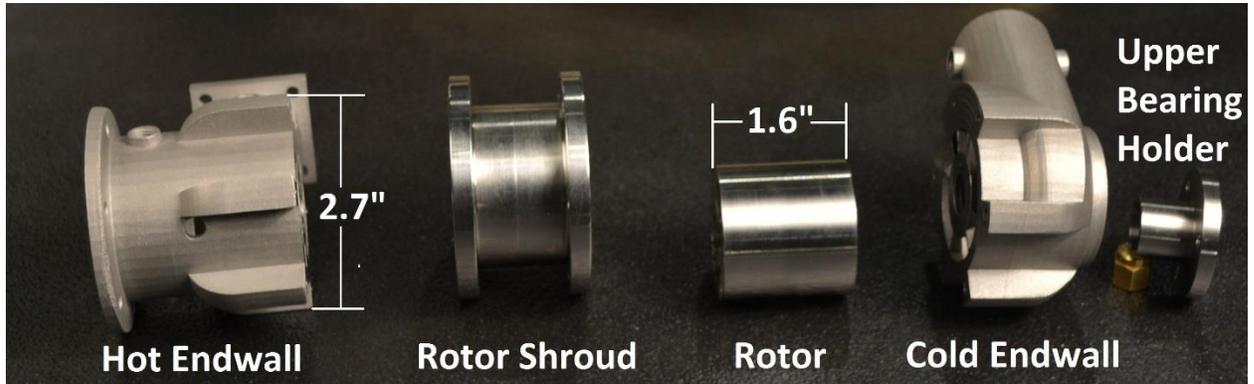

Figure 39: Assembly of manufactured parts

Currently, the rotors are mounted on the shafts and the assembly is being balanced for the design point speed of 34,500 rpm. All supporting tubing and ducting to route the heated air from the facility to the PWS and through the proper tubing containing the measuring equipment has been fabricated and is ready to receive the PWS. Once the rotors are balanced, one of the rotors will be mounted in the cold endwall and the overall device will be assembled. In order for the device to operate properly, the clearances between the rotor and the two endwalls must be checked carefully, and the shroud and shaft may be modified to ensure the proper tolerances are achieved.

V. Conclusions and Recommendations

As unmanned aerial systems become a more common tool for surveillance of enemies on the battlefield, there will continue to be a desire for more portable systems with increased capabilities. The small engines used in the smallest reconnaissance aircraft of today are based on engines from small hobbyist aircraft that are meant to be flown very close to sea level. These engines are not highly efficient when operated with intake manifold pressures much lower than that of sea level standard conditions.

Research has demonstrated the marked decrease in performance for operation of these small engines at decreased intake pressures. Methods such as turbocharging and supercharging do exist to increase the intake manifold pressure and volumetric efficiency of internal combustion engines. Such methods have been shown to be highly effective for relatively large engines. However, due to the inefficiencies associated with scaling down a compressor to a size appropriate for small engines such as the 95 cc Brison, conventional turbochargers and superchargers are generally ineffective.

If a supercharger could be designed that could efficiently boost the intake manifold air pressure of a small UAS engine from the low pressures experienced at altitude to that of one standard atmosphere or better, the engine would be able to operate as if it were near the ground where it was designed to operate. This would allow these small surveillance aircraft to fly much higher and potentially carry a larger payload than is currently possible with an un-boosted engine. This performance enhancement would offer a greater field of view for the surveillance equipment onboard, as well as a reduced ability for the aircraft to be observed from the ground. A portable, stealthy, high-performance surveillance aircraft

offers a huge potential advantage in a combat situation where stealth is a key component to mission success.

Since a PWS does not use a compressor to charge the intake air, it is highly possible that a more efficient supercharger in the form of a PWS could be a viable option for improving the performance of small engines at high altitude. Future testing of the PWS prototype designed in this project will help to confirm or nullify the efficiency of such a small-scale device. The efficiency gains computed for the CFD simulation of this PWS would represent great advancement in the field of supercharging very small internal combustion engines.

V.1 Research Goals

Throughout the research process, this thesis was focused on achieving four main objectives as outlined in Chapter I. These objectives were as follows;

1. Improvement of the test apparatus of Smith et al. [5] for the purpose of further Comprex® PWS testing with improved temperature capability

2. Validation of the NASA GRC CFD code developed by Paxson [6] applied to a reverse-flow wave rotor of the type designed in this project

3. Theoretical design and computational simulation of a small scale PWS sized for the 95 cc Brison engine

4. Manufacturing, and mechanical integration of the scaled PWS into a test apparatus for the purpose of testing the scaled model against the CFD code used

In order to improve the testing facility developed by Smith et al. [5], the temperature capability of the rig was improved through the addition of insulation to the lines supplying heated air to the EI tube, as well as adding small heaters to this tube. This enabled testing of the Comprex® at elevated temperatures of up to 1035 R, as opposed to the previously attained maximum temperature of 883 R with the test rig in its old configuration. A new automotive MAF sensor was also adapted to the test rig in order to help improve upon the inaccuracy of the one used by Smith et al. [5]. These improvements helped in the accomplishment of Objective 1.

With the improved Comprex® testing facility, further testing was accomplished and data was taken. Several data points were repeated from Smith et al. [5] in order to ensure repeatability of his measurements. With the old rig, Smith et al. [5] were never able to properly balance the mass flows of the Comprex® in a manner that resembled the proper operation of the device. With the increased temperature capabilities, a balanced operating point was pursued and eventually found. This point was then simulated using the NASA GRC CFD code, and the calculated parameters were found to have good agreement with the measured values of those parameters. This validation inspired confidence in the code's ability to predict Pressure Wave Supercharger performance, which allowed progression to Objective 3 of the research.

Using the process outlined by the designers of the Comprex®, a small-scale Pressure Wave Supercharger was designed for application to a Brison 95 cc engine on a small unmanned aerial system. The design process began by performing mathematical calculations pertaining to the size of the rotor and the ports in the endwalls of the wave

rotor. The code was then used to simulate the performance of the design. During the first design iteration, it was discovered that the design would not yield a sufficient mass flow of air that had been calculated for the engine. This design was improved upon by expanding the rotor cells until the code indicated that the required performance was satisfied for the design point. Simulations of the rotor at operating conditions other than the design point were also performed in order to analyze the overall performance of the device. With the device properly simulated, Objective 4 of the research was pursued.

In order to begin the design process, Computer Aided Design models of the individual parts were made and virtually assembled to ensure proper mechanical assembly and working order. With the parts modeled, materials were selected and the designs were sent out for manufacturing by direct metal laser sintering. In order to test the device that had been designed, a test rig was needed similar to the one Smith et al. [5] had designed. Such a test rig was designed and the scaled PWS is being mechanically integrated with it in order to compare its measured performance against that predicted by the code.

V.2 Conclusions of Research

Although the construction of the test rig is not yet complete, initial simulations indicate that the down-sized PWS designed in this study should be able to improve the Manifold Absolute Pressure of the Brison 95 cc engine enough to operate at much higher altitudes than are currently possible on the naturally aspirated engine. The results of Husaboe [2] have shown that the Brison loses approximately 35% in horsepower from its sea level performance when it flies at 15,000 ft. This altitude represents an inlet condition

99

of 466 R, 8.297 psia. Simulations of the scaled PWS at the design point indicate a boost in inlet air pressure of a factor of 2.622. This would result in the Brison 95 cc engine flying at 15,000 ft with an intake manifold pressure of approximately 22 psia. This boost in pressure will allow the engine to operate as if it were flying much closer to the ground and should reverse the loss in power associated with increasing altitude. In theory, the addition of the PWS should generate additional power at altitude than the base engine would produce at sea level.

Most Pressure Wave Superchargers in the past have been designed for use on automotive diesel engines due to the smaller variability in engine speed compared to a gasoline engine during normal operation. Since the rotor of the PWS is coupled to the crankshaft, a lack of change in engine speed allows the wave rotor to operate near its design point during most of the time when the supercharger is in operation. For operating off-design the performance of the PWS tends to suffer, although the addition of endwall pockets helps to mitigate the negative effects of changing the rotor speed on the wave structure to some extent. Since a reconnaissance aircraft is designed to circle an area for long periods of time at relatively constant airspeed and engine rpm, the use of a PWS should be practical for this application. Simulations show that the endwall pockets incorporated in the design of the small scale PWS will allow off-design operation with a minimal drop in performance.

Further research will enable better design of future Pressure Wave Superchargers of this scale by indicating the extent of the losses present for a compressor of this size. Traditional axial and centrifugal compressors are very inefficient for the low mass flows

associated with small scale engines like the Brison 95 cc. Since a PWS does not make use of a traditional compressor and instead uses pressure waves to compress air, it has the potential to avoid many of the scaling issues that lead to highly inefficient compression. One source of inefficiency in small-scale turbochargers is the extremely high shaft speeds of around 150,000 rpm or higher required for adequate compression from such a small compressor. The design shaft speed of the scaled PWS designed in this project is 34,500 rpm, leading to reduced bearing friction and viscous friction than would otherwise be present with higher speeds. Blade tip effects also need not be considered since there is no compressor blade in a PWS.

Small engines like the 95 cc Brison that are used on very small unmanned aerial systems are typically designed for hobbyist aircraft that do not operate at high altitudes. Once tested and fully integrated, the PWS design outlined in this thesis will boost the intake manifold pressure of the Brison engine enough to overcome the power loss associated with engine operation at higher altitudes as illustrated by Husaboe et al [2]. This performance enhancement will increase the mission capabilities of the small UAS aircraft that will utilize wave rotor technology by allowing these aircraft to fly higher and faster than previously possible.

V.3 Significance of Research

One method of increasing the stealth capability of small UAS aircraft is to decrease the noise level so that it will be less noticeable near the ground, although this would not

make the aircraft harder to see. Another method would be to increase the altitude of the aircraft so it is harder to see and hear on the ground. Decreasing the noise level of an internal combustion engine generally involves a more restrictive exhaust system, usually resulting in a drop in fuel efficiency and power. Since the majority of the noise made by the aircraft comes from the shock waves generated at the tips of the propeller, decreasing the noise level of the engine would likely have little effect on its observability. This leaves the designer with the problem of improving the engine's performance to allow for flying at higher altitude.

The scaled Pressure Wave Supercharger designed in this thesis will increase the power output of a very small engine while maintaining a level of efficiency that is acceptable for practical implementation of such a device. The research presented in this paper suggests that a properly designed small-scaled Pressure Wave Supercharger will boost the power output of the Brison 95 cc engine by up to 50% by increasing the Manifold Absolute Pressure from the low pressures present at high altitudes, back to one standard atmosphere or better. Due to the exceptionally high shaft speeds needed for a similarly scaled turbocharger or supercharger to provide a similar performance boost, these devices encounter a large drop-off in efficiency for the low mass flows required making them impractical for use on such a small engine.

V.4 Recommendations for Future Research

Since the construction of the small-scale test rig is already well underway, the natural direction for future research in this project is very straight-forward. Future research should progress in three major phases. First, the small test rig should be completed and made operational for the purpose of testing the scaled wave rotor. Once the code and the design have been validated at this scale, the second phase of research should be to couple the scaled PWS to the actual Brison 95 cc engine for further testing. Third, the design should be improved based on the results of testing. Accomplished in the order specified above, these phases should lead to a design that will be improved thermodynamically as well as physically.

Once the test rig is completed and the major problems with the rig are fully understood and fixed, testing should be performed in order to validate the CFD simulations. This testing will also give a better idea of what the loss models should be to include the endwall pockets, endwall leakage, frictional losses, boundary layer losses, and heat transfer out of the passages. This research will not only prove whether or not turbo-normalization of a very small engine through the use of a PWS is possible and worthwhile, but it will also improve the CFD model, and therefore improve the ability of the designer to predict the performance of a PWS of this scale. The lessons learned here and in Phase 2 of the proposed future research will be very important for the work proposed for the third phase.

V.5 Summary

The results of the research conducted thus far are very promising in terms of projected performance for a small-scale Pressure Wave Supercharger. The CFD code developed by the Glenn Research center was used to validate its use as an accurate simulation tool for the Comprex®, a larger Pressure Wave Supercharger. The successful validation of the code encouraged its use for simulating very similar devices of much smaller scale. This thesis utilizes the CFD code as a design tool for developing a PWS for a 95 cc engine that is twenty times smaller than the 2.0 liter diesel engine that the Comprex® was designed for. Since a PWS uses pressure waves to compress air as opposed to a spinning compressor, many of the losses associated with scaling down a conventional turbo-normalization device are not relevant for scaling a wave rotor. This unique characteristic of wave rotors lends itself to use as a compressor on a very small scale for relatively small mass flows.

This thesis details the process for designing a Pressure Wave Supercharger scaled down for use on a 95 cc Brison engine that is used as the power plant for small unmanned aerial systems. Wave rotor performance is heavily dependent on achieving the proper rotor speed, so operation of the wave rotor outside of the design point often leads to very poor performance. The rotor is commonly coupled to the crankshaft in order to control the speed and since the crankshaft speed of an internal combustion engine varies greatly for most uses, wave rotors are not a popular solution for supercharging engines. However, the addition of endwall pockets can help mitigate the loss of performance for operation of the wave rotor slightly off of the design speed. Simulations indicate that the scaled PWS

designed in this research study should be able to provide a 50% performance boost for rotor speeds that differ by at least 30% different from the design speed.

A similar test program to that run for the Comprex® should be completed. This testing program will enable better design of future Pressure Wave Superchargers for small engines by enabling a better understandings of the loss mechanisms that drive wave rotor performance for devices of such a small scale. This design process could be applied to a multitude of UAS engines in order to boost their performance. This innovative technology could help to improve the performance of small surveillance aircraft so that they could fly higher than ever before, greatly improving their stealth, speed, field of view, and overall flexibility to perform missions in more extreme circumstances.

Bibliography

1.   Crosbie, S., Polanka, M., Litke, P., and Hoke, J. "Increasing Reliability of a Small 2-Stroke Internal Combustion Engine for Dynamically Changing Altitudes." AIAA Paper. AIAA 2012-0950. 50th AIAA Aerospace Sciences Meeting including the New Horizons Forum and Aerospace Exposition, 09-12 January 2012, Nashville, TN.

2.   Husaboe, T., Rittenhouse, J., Polanka, M., Litke, P., and Hoke, J. "Small Internal Combustion Engine Dependence on Inlet Pressure and Temperature at Altitude." AIAA Paper. DOI: 10.2514/6.2013-3649. 14-17 July, 49th AIAA/ASME/SAE/ASEE Joint Propulsion Conference, San Jose, CA. 2013.

3.   R. van Basshuysen and F. Schafer. *Internal Combustion Engine Handbook: Basics, Components, Systems, and Perspectives*. Society of Automotive Engineers International. 2004, Warrendale, PA.

4.   P.K. Doerfler. "Comprex Supercharging of Vehicle Diesel Engines." BBC Brown, Boveri & Co., Ltd. Automotive Engineering Congress and Exposition, Paper #750335. February 24-28, 1976. Detroit, MI.

5.   Smith, B., Polanka, M., Paxson, D., and Hoke, J. 2012. "Scaling Study of Wave Rotor Turbo-Normalization of an Combustion Engine." AIAA JPC Paper. AIAA 2012-3837. 48th AIAA/ASME/SAE/ASEE Joint Propulsion Conference and Exhibit, 30 July-01 August, 2012. Atlanta, GA.

6.   D. E. Paxson. "A General Numerical Model for Wave Rotor Analysis." National Aeronautics and Space Administration Lewis Research Center, NASA Technical Memorandum 105740. Cleveland, OH.

7.   Hirecaga, M., Iancu, F., Muller, N., "Wave Rotors Technology and Applications." Scientific Bulletin of the "Politehnica" University of Timisoara Transactions on Mechanics Special Issue, The 11th International Conference on Vibration Engineering, September 27-30, 2005. Timisoara, Romania.

8.   L. Fluckiger, S. Tafel, and P. Spring. "Pressure Wave Supercharged Spark-Ignition Engines. MTZ worldwide." Volume 67, Issue 12, pp 6-9.

9.   J.D. Mattingly. *Elements of Propulsion: Gas Turbines and Rockets*. American Institute of Aeronautics and Astronautics, 2006. Reston, VA.

10. Zehnder, G., and Mayer, A. "Comprex® Pressure-Wave Supercharging for Automotive Diesels—State-of-theArt." BBC Brown, Boveri & Co., Ltd. International Congress and Exposition, Paper #840132, February 27-March 2, 1984. Detroit, MI.

11. Hussain, J., Palaniradja, K., Alagumurthi, N., Manimaran, R. "Effect of Exhaust Gas Recirculation (EGR) on Performance and Emission of a Compression Ignition Engine with Staged Combustion (Insertion of Unburned Hydrocarbon)." International Journal of Energy Engineering. 2012; 2(6): 285-292.

12. G. Gyarmathy. "How Does a Comprex® Pressure-Wave Supercharger Work?" SAE Technical Paper 830234, International Congress and Exposition, Feb 28-Mar 4, 1983. Detroit, MI.

13. P. Akbari, R. Nalim and N. Mueller. "A Review of Wave Rotor Technology and Its Applications." American Society of Mechanical Engineers Journal of Engineering for Gas Turbines and Power, 2006.

14. Berchtold, M., and Gardiner, F.J. "The Comprex: A New Concept of Diesel Supercharging." ASME Paper 58-GTP-16. 1958.

15. "1981 126 CK." *Scuderia Ferrari*. Ferrari Formula 1 Website. N.p., n.d. Web. 27 Jan. 2014 <http://formula1.ferrari.com/cars/126-cx>.

16. Pranav, S. "Wave Rotor Test Rig Design Procedure for Gas Turbine Enhancement." University Microfilms International, 2008. Ann Arbor, MI.

17. J. Wilson, G. Welch, and D. Paxson. "Experimental Results of Performance Tests on a Four-Port Wave Rotor." American Institute of Aeronautics and Astronautics (AIAA) Aerospace Sciences Meeting and Exhibit Paper #2007-1250. 2007.

18. J.D. Anderson. *Modern Compressible Flow: With Historical Perspective*. McGraw-Hill. 1982. New York, NY.

19. Weber F., Guzella, L., and Onder, C. "Modelling of a Pressure Wave Supercharger including external exhaust gas recirculation." Institution of Mechanical Engineers Part D Journal of Automobile Engineering. DOI:10.1243/0954407021529057. 2002.

20.   "Final Rulemaking to Establish Light-Duty Vehicle Greenhouse Gas Emission Standards and Corporate Average Fuel Economy Standards." United States Environmental Protection Agency Joint Technical Support Document. EPA-420-R-10-901. April 2010.

21.   R. Fried, F. Jaussi, and F Spinnler. "Internal Combustion Engine with a Pressure Wave Supercharger." U.S. Patent US4723525. 11 June 1986.

22.   Okamoto, K., Nagashima, T., and Teramoto, S. "Multi-Passage Gasdynamic Interactions in Wave Rotor." 24th International Congress of the Aeronautical Sciences. ICAS 2004-7.10.3. 29 August-03 September, 2004.

REPORT DOCUMENTATION PAGE

Form Approved
OMB No. 0704–0188

1. REPORT DATE (DD–MM–YYYY) 27-03-2014	2. REPORT TYPE Master's Thesis	3. DATES COVERED (From — To) Oct 2012 - Mar 2014

4. TITLE AND SUBTITLE Design and Simulation of a Pressure Wave Supercharger for a Small Two-Stroke Engine	5a. CONTRACT NUMBER
	5b. GRANT NUMBER
	5c. PROGRAM ELEMENT NUMBER
6. AUTHOR(S) Mataczynski, Mark R, 2Lt, USAF	5d. PROJECT NUMBER
	5e. TASK NUMBER
	5f. WORK UNIT NUMBER

7. PERFORMING ORGANIZATION NAME(S) AND ADDRESS(ES) Air Force Institute of Technology Graduate School of 2950 Hobson Way WPAFB OH 45433-7765	8. PERFORMING ORGANIZATION REPORT NUMBER AFIT-ENY-14-M-34

9. SPONSORING / MONITORING AGENCY NAME(S) AND ADDRESS(ES) Air Force Research Laboratory, Propulsion Directorate, Combustion Sciences Branch Attn: Frederick R. Schauer 2464 C St., Bldg. 20071A, Rm. 201 Wright Patterson AFB, OH 45433-7251 (937) 785-6462	10. SPONSOR/MONITOR'S ACRONYM(S) AFRL/RQTC
	11. SPONSOR/MONITOR'S REPORT NUMBER(S)

12. DISTRIBUTION / AVAILABILITY STATEMENT

DISTRIBUTION STATEMENT A: APPROVED FOR PUBLIC RELEASE; DISTRIBUTION UNLIMITED.

13. SUPPLEMENTARY NOTES

This material is declared a work of the U.S. Government and is not subject to copyright protection in the United States.

14. ABSTRACT

As small, Remotely Piloted Aircraft become more prevalent as aerial observation platforms in the modern era, there will continue to be a desire to improve their capabilities. The lowered pressures associated with high altitude have an adverse impact on the performance of the small engines that are commonly used to propel small aircraft. The most desirable method of recovering the performance lost as a result of engine operation at high altitude is the integration of a forced induction device. Due to its unique characteristics, a special type of wave rotor called a Pressure Wave Supercharger has the potential to avoid many scaling-related losses, allowing it to operate efficiently as a forced induction device for very small engines. This thesis outlines the successful design and computational simulations performed in the development of a Pressure Wave Supercharger for a 95 cc Brison engine. A NASA quasi one-dimensional CFD code was used to produce computational predictions for the performance of a Comprex® Pressure Wave Supercharger and compare these predictions against the measured performance. This code was then used to design a scaled down version of the Comprex® for use on the 95 cc Brison engine. This design was modeled using Computer Aided Design and the parts were manufactured. A test rig was also designed for the purpose of testing the scaled Pressure Wave Supercharger. This device will improve the performance of small two-stroke engines flying at high altitudes by boosting the intake manifold pressure back to one standard atmosphere or better. This will allow very small unmanned aerial systems operated by the Air Force to function at higher altitudes, thus improving their capabilities and mission effectiveness.

15. SUBJECT TERMS

Pressure, PWS, RPA, Supercharger, Two-stroke, UAS, Wave, Rotor.

16. SECURITY CLASSIFICATION OF:			17. LIMITATION OF ABSTRACT	18. NUMBER OF PAGES	19a. NAME OF RESPONSIBLE PERSON Dr. Marc D. Polanka / ENY
a. REPORT U	b. ABSTRACT U	c. THIS PAGE U	UU	122	19b. TELEPHONE NUMBER (Include Area Code) (937) 785-3636 x4714 marc.polanka@afit.edu

Standard Form 298 (Rev. 8–98)
Prescribed by ANSI Std. Z39.18